Evaluating a space-based indicator of surface ozone-NO_x-VOC sensitivity over mid-latitude source regions and application to decadal trends

Xiaomeng Jin[1], Arlene M. Fiore[1], Lee T. Murray[2], Lukas C Valin[3], Lok N. Lamsal[4], Bryan Duncan[4], K. Folkert Boersma[5,6], Isabelle De Smedt[7], Gonzalo Gonzalez Abad[8], Kelly Chance[8], Gail S. Tonnesen[9]

1. Department of Earth and Environmental Sciences and Lamont-Doherty Earth Observatory of Columbia University, Palisades, NY, USA
2. Department of Earth and Environmental Sciences, University of Rochester, Rochester, NY, USA
3. U.S. EPA Office of Research and Development, Research Triangle Park, NC, USA
4. NASA Goddard Space Flight Center, Greenbelt, Maryland, USA
5. Royal Netherlands Meteorological Institute, De Bilt, The Netherlands
6. Wageningen University, Wageningen, The Netherlands
7. Belgian Institute for Space Aeronomy (BIRA-IASB), Brussels, Belgium
8. Harvard-Smithsonian Center for Astrophysics, Cambridge, MA, USA
9. United States Environmental Protection Agency, Region 8, 1595 Wynkoop Street, Denver, CO 80202, USA

For submission to *Journal of Geophysical Research: Atmospheres*

Abstract

Determining effective strategies for mitigating surface ozone (O_3) pollution requires knowledge of the relative ambient concentrations of its precursors, NO_x and VOCs. The space-based tropospheric column ratio of formaldehyde to NO_2 (FNR) has been used as an indicator to identify NO_x-limited versus NO_x-saturated O_3 formation regimes. However, quantitative use of this indicator ratio is subject to three major uncertainties: 1) the split between NO_x-limited and NO_x-saturated conditions may shift; 2) the ratio of the vertically integrated column may not represent the near-surface environment; 3) satellite products contain errors. We use the GEOS-Chem global chemical transport model to evaluate the quantitative utility of FNR observed from the Ozone Monitoring Instrument over three northern mid-latitude source regions. We find that FNR in the model surface layer is a robust predictor of the simulated near-surface O_3 production regime. Extending this surface-based predictor to a column-based FNR requires accounting for differences in the HCHO and NO_2 vertical profiles. We compare four combinations of two OMI HCHO and NO_2 retrievals with modeled FNR. The spatial and temporal correlations between the modeled and satellite-derived FNR vary with the choice of NO_2 product, while the mean offset depends on the choice of HCHO product. Space-based FNR indicates that the spring transition to NO_x-limited regimes has shifted at least a month earlier over major cities (e.g. New York, London, Seoul) between 2005 and 2015. This increase in NO_x sensitivity implies that NO_x emission controls will improve O_3 air quality more now than it would have a decade ago.

1 Introduction

Surface ozone (O_3), the main component of photochemical smog, has adverse effects on public health [*Kampa and Castanas*, 2008], agriculture [*Van Dingenen et al.*, 2009] and ecosystems [*Yue and Unger*, 2014]. The global premature mortality rate due to O_3 pollution is estimated at 0.8 million/year [*Lelieveld et al.*, 2013]. Surface O_3 formation in urban areas is non-linearly dependent on the availability of two classes of O_3 precursors: oxides of nitrogen (NO_x) and volatile organic compounds (VOCs). That is, depending on local relative abundances of NO_x to VOCs, O_3 formation can be mitigated by reducing NO_x emissions (NO_x-limited regime), or by reducing VOC emissions (NO_x-saturated or VOC-limited or radical-limited regime). At regional and global scales, O_3 production is largely NO_x-limited, though urban areas with high NO_x emissions are frequently NO_x-saturated.

The non-linear dependence of surface O_3 on precursor emissions poses challenges to effective mitigation of surface O_3. *Simon et al.* [2015] find that U.S. summertime O_3 decreases with its precursor emissions in recent decades, but wintertime O_3 increases in urban areas as NO titration declines. Urban areas with NO_x-saturated O_3 production chemistry should be transitioning to NO_x-limited chemistry following the substantial nationwide NO_x emission reductions implemented since the late 1990s [*Pusede et al.*, 2015]. NO_x emissions decreased by 27% over Europe in the past decade, and the overall O_3 distribution narrowed [*Guerreiro et al*., 2014; *Lefohn et al*., 2017]. In China, controls on anthropogenic NO_x emissions are being implemented [*Gu et al*., 2013; Liu *et al*., 2016; *Souri et al*., 2017], but surface O_3 may increase due to the dominance of VOC-limited ozone formation regimes [*Liu et al.*, 2013; *Jin and Holloway*, 2015; *Lefohn et al*., 2017].

O_3 sensitivity to precursor emissions has been derived from models using various approaches including emission perturbation simulations [*Jacob et al.*, 1995; *Wu et al.*, 2009; *Tonnesen and Dennis*, 2000], O_3 source apportionment [*Dunker et al*., 2002; *Cohan et al.*, 2005; *Li et al.*, 2012], and adjoint modeling [*Schmidt et al*., 2003; *Hakami et al.*, 2006; *Zhang et al*., 2009]. Model uncertainties, including the possibility of compensating errors, could lead to erroneous estimates of O_3 sensitivity despite accurate simulation of O_3 concentrations [*Sillman*, 1995; *Tonnesen and Dennis*, 2000]. Furthermore, the sensitivity is non-linearly dependent on the magnitude of the emission perturbation [*Wu et al.*, 2009; *Fu et al.*, 2012].

Sillman [1995] showed that the relationships of NO_y to O_3, H_2O_2 to HNO_3, and HCHO to NO_y reflect the processes that determine the non-linear sensitivity of O_3 to VOC and NO_x precursor emissions, which has been further examined in models and measurements [*Jacob et al.*, 1995; *Tonnesen and Dennis*, 2000; *Hammer*, 2002; *Stein et al.*, 2005]. The relative ambient concentrations of HCHO and NO_y or NO_2 reflect the reactivity-weighted concentrations of VOC and NO_x, respectively, and thus indicate how O_3 will respond to changes in NO_x and VOC emissions [*Sillman*, 1995; *Valin et al*., 2016]. *Tonnesen and Dennis* [2000] suggest HCHO/NO_2 is more useful than HCHO/NO_y because both HCHO and NO_2 have short lifetimes (~ hours), and their ratio better represents the competition between OH reaction with VOC versus NO_2.

Martin et al. [2004a] first applied the indicator ratio to Global Ozone Monitoring Experiment (GOME) retrievals of tropospheric columns of HCHO and NO_2 with a spatial

resolution of 80 × 40 km^2, and proposed that the transition from NO_x-saturated to NO_x-limited occurs when HCHO/NO_2 equals 1, thereby diagnosing the O_3-NO_x-VOC sensitivity across the globe from space. This work has been refined and extended to Ozone Monitoring Instrument (OMI) products to characterize O_3 sensitivity over the U.S.A. [*Choi et al.*, 2012; *Duncan et al.*, 2010; *Chang et al.*, 2016] and East Asia [*Jin and Holloway*, 2015; *Souri et al*., 2017]. The finer spatial resolution of OMI (up to 13×24 km^2) better captures the urban-rural gradient of O_3 sensitivity. In addition, the OMI overpass time (~1:45 PM) is better suited to detect the sensitivity of ozone production during the afternoon, when O_3 photochemical production peaks, and when the boundary layer is deepest and the solar zenith angle is small, maximizing instrument sensitivity to HCHO and NO_2 in the lower troposphere.

Table 1 summarizes previous studies that use HCHO/NO_y or HCHO/NO_2 as indicators for O_3-NO_x-VOC sensitivity. While previous studies have demonstrated the potential of the space-based indicator ratio to identify the O_3 sensitivity to NO_x *vs.* VOC emission controls, the quantitative application of space-based HCHO/NO_2 is subject to three major uncertainties. First, different mechanisms and meteorological conditions, such as humidity, temperature and dry deposition rates can affect the relationship of O_3 production to HCHO/NO_2 [*Sillman*, 2002; *Vogel et al.*, 2007; *Liu et al.*, 2010]. Second, satellite observations measure the vertically integrated column density, which differs from the mixing ratio near the surface, of most relevance to air quality management. Variations in the vertical distribution of HCHO relative to that of NO_2 also alter the relationship between the column and surface ratios [*Martin et al.*, 2004b]. Third, even if column-based HCHO/NO_2 is a useful indicator of surface O_3 sensitivity, satellite retrievals are subject to large uncertainties from measurement errors, surface reflectivity, cloud effects, profile shape and aerosol effects [*Boersma et al.*, 2004; *Lin et al.*, 2014]. *Duncan et al.* [2010] and *Martin et al.* [2004b] derive the ozone production regime thresholds (i.e., the range of values over which the transition occurs from NO_x-saturated to NO_x-limited) from modeled column densities, assuming that modeled column densities match what is retrieved from space. Inter-model comparison of indicator ratios, however, shows large disagreements between satellite products and models [*Campbell et al.*, 2015]. *Zhu et al.* [2016] suggest HCHO satellite retrievals are biased low relative to aircraft data, with the extent of this underestimate varying by product. If HCHO is biased low, the extent of VOC-limited regimes will be overestimated.

We investigate these uncertainties by first evaluating the quantitative utility of the indicator ratio $HCHO/NO_2$ (hereafter FNR) observed from OMI over three mid-latitude source regions: North America (22 °N - 50 °N, 75 °W - 120 °W), Europe (35 °N - 60 °N, 10 °W - 30 °E) and East Asia (20 °N - 50 °N, 100 °E - 140 °E). Relative to a multi-year (2006 - 2012) base-case GEOS-Chem simulation, we conduct two perturbation simulations that separately reduce NO_x and VOC emissions globally by 20% to examine the ability of FNR to detect the surface O_3 sensitivity to precursor emissions (Section 3.1). Using the 3-D distribution of NO_2 and HCHO archived from GEOS-Chem, we examine the surface-to-column relationships of FNR and their spatial and temporal variations (Section 3.2). The model-derived surface-to-column relationships are then applied to determine the column-based regime threshold values. We then compare four combinations of two OMI HCHO products and two OMI NO_2 products with the GEOS-Chem simulations (Section 3.3). Finally, we investigate decadal trends in surface O_3 sensitivity over northern mid-latitude polluted regions from 2005 to 2015 using the fine OMI products with 0.25° resolution (Section 4).

2 Data and Methods

2.1 OMI Products

OMI is on board the NASA EOS Aura satellite at ~705 km altitude in a sun-synchronous orbit with 98° inclination [*Levelt et al.*, 2006]. OMI is a nadir-viewing UV/visible spectrometer, providing daily, near global coverage with a local equator crossing time of ~1:45 PM. OMI covers two UV region (264 - 311 nm and 307 - 383 nm) and one VIS region (349 - 504 nm) with a spectral resolution between 0.42 to 0.63 nm and a spatial resolution of up to 13 × 24 km^2 at nadir [*Levelt et al.*, 2006].

2.1.1 OMI Tropospheric NO_2

We use two Level-2 OMI NO_2 satellite retrieval products: the Level-2 standard operational NO_2 Product ($OMNO_2$ SP, version 2.1) developed at NASA/Goddard Space Flight Center [*Bucsela et al.*, 2013], and the Dutch NO_2 product (DP) developed at KNMI, the Royal Netherlands Meteorological Institute (DOMINO DP, v2.0) [*Boersma et al.*, 2011]. Retrieval of tropospheric NO_2 column density involves three major steps: (1) spectral fitting to obtain a raw NO_2 slant column density; (2) separation of tropospheric and stratospheric columns; and (3) conversion from slant column to vertical column density. NASA SP and DOMINO DP differ in

(2) and (3) [*Bucsela et al.*, 2013; *Boersma et al.*, 2011]. The air mass factor (AMF, the ratio of the slant column to the vertical column density) can be expressed as the vertical integral of the contribution of each layer to the column divided by the vertical column [*Boersma et al.*, 2011]:

$$AMF = \frac{\sum_l m_l(\mathbf{b}) \cdot x_{a,l}}{\sum_l x_{a,l}} \quad (1)$$

where $m_l(\mathbf{b})$ is the atmospheric scattering weight that is a function of satellite viewing geometry, cloud pressure, cloud radiance fraction, surface pressure and reflectivity, and $x_{a,l}$ is the sub-column from the a priori profile for layer *l*. Scattering weights are included in the NASA Level-2 SP. DP provides averaging kernels (AK) as an alternative, which is equal to $m_l(\mathbf{b})$/AMF [*Eskes and Boersma*, 2003]. A recent study estimates a structural uncertainty of 42% for AMF over polluted regions resulting from different priori trace gas profiles, surface albedo and cloud parameters applied for AMF calculation [*Lorente et al*., 2017]. In this study, we calculate the tropospheric AMF (AMF_{trop}) consistently for both DP and SP by using 1-hour average GEOS-Chem modeled NO_2 profiles sampled each day at the OMI overpass time, which enables direct comparison between GEOS-Chem and the OMI products [*Boersma et al*., 2016]. We use the stratospheric NO_2 columns and AMFs provided with the data products. We calculate the NO_2 tropospheric column density at each pixel as the difference between the total and the stratospheric slant column density:

$$V_{trop} = \frac{S - S_{stra}}{AMF_{trop}} \quad (2)$$

where V_{trop} is tropospheric column density; AMF_{trop} is the tropospheric AMF; S is the de-striped total slant column density; S_{stra} is the stratospheric slant column density. For DP, we use the TM4 assimilated stratospheric slant column density (S_{stra}) included in the product. For SP, S_{stra} is calculated as the product of the stratospheric column density (V_{strat}) and the stratospheric AMF (AMF_{strat}) included in the product. We select individual observations with cloud radiance fraction lower than 30%, solar zenith angle smaller than 85°, and only those unaffected by row anomalies (http://www.knmi.nl/omi/research/product/rowanomaly-background.php) [*Dobber et al*., 2008]. The overall uncertainty of the OMI SP and DP retrievals is on the order of ~10^{15} molecules/cm^2 over polluted areas (20% - 30% of the retrieved quantity) [*Boersma et al.*, 2011; *Bucsela et al.*, 2013]. While the effects of aerosols on satellite retrievals are not included explicitly, such effects are accounted for implicitly via cloud retrievals being sensitive to the scattering effects of

aerosols, though such corrections may not work well for extreme aerosol loading and highly absorbing aerosol mixtures [*Lin et al.*, 2014, 2015; *Lorente et al.*, 2017]. Evaluation of the OMI SP NO_2 (version 2.1) with ground-based and aircraft data shows that OMI products generally agree with *in situ* measurements over the U.S.A. within ±20% [*Lamsal et al.*, 2014]. *Marchenko et al*. [2015] suggest that the OMI retrieved slant column density is overestimated by 10 to 40%; improvements in slant column density have been made to the Version 3 NASA products, but are not yet included in DP. We use SP from Version 2.1 for the sake of consistency with DP.

2.1.2 OMI HCHO

We use two Level-2 OMI HCHO retrieval products: NASA's standard product developed by the Smithsonian Astrophysical Observatory (SAO) team (OMI-SAO, v3.0) [*González Abad et al.*, 2015], and the Belgian Institute for Space Aeronomy (BIRA-IASB) retrieval (OMI-BIRA, v14) [*De Smedt et al.*, 2015]. HCHO slant columns are estimated via spectral fitting in near ultra-violet (UV) regions. The OMI-SAO retrieval of slant columns differs from BIRA-IASB in the absorption cross sections for HCHO, BrO and NO_2 [*González Abad et al.*, 2015; *De Smedt et al.*, 2015]. We convert slant columns to vertical columns ($\Omega_{\text{HCHO-BIRA}}$ and $\Omega_{\text{HCHO-SAO}}$) via the AMF (Equation 1) provided with the products. For direct comparison, we use 1-hour average GEOS-Chem HCHO profiles sampled each day at the OMI overpass time as the a priori vertical profiles. The scattering weights are based on the scalar LIDORT radiative transfer model (v3.3) for OMI-BIRA, and the VLIDORT for OMI-SAO (v2.4) [*Spurr*, 2008]. Latitude-dependent biases due to unresolved spectral interferences are pronounced for weak absorbers such as HCHO. OMI-BIRA and OMI-SAO products deal with the spectral interference differently: OMI-BIRA product employs a two-step across-track and zonal reference sector correction to normalize the HCHO slant columns [*De Smedt et al.*, 2015], and OMI-SAO product applies a post-processing normalization for the vertical column density using a model reference sector over the remote Pacific Ocean [*González Abad et al.*, 2015]. Similar to NO_2, the effects of aerosol are not accounted for explicitly for both retrievals. We select observations with cloud radiance fraction less than 30%, solar zenith angle smaller than 70°, and unaffected by row anomalies following the criteria suggested in *De Smedt et al.* [2015]. The overall error of the monthly average HCHO column is about 30% for both products [de *Smedt et al.*, 2008, 2012; *González Abad et al.*, 2015].

2.1.3 OMI HCHO/NO_2

Daily Level-2 OMI NO_2 and OMI HCHO data from 1 January 2005 to 31 December 2012 are re-gridded to the GEOS-Chem model grid for direct comparison with the model simulations. In order to reduce the random errors in the satellite retrievals, we first calculate seven-day average tropospheric NO_2 and HCHO column densities (Ω_{GC_NO2} and Ω_{GC_HCHO}). Negative columns may occur as a result of minimizing residuals during the spectral fitting below the satellite detection limit and are included when constructing seven-day averages [*Boeke et al.*, 2011]. We calculate four combinations of the O_3 sensitivity indicator ratio (FNR) by taking the ratio of seven-day average Ω_{HCHO} to Ω_{NO2}: 1) $\Omega_{HCHO\_SAO}/\Omega_{NO2\_SP}$ (FNR_{OMI_SS}); 2) $\Omega_{HCHO\_BIRA}/\Omega_{NO2\_SP}$ (FNR_{OMI_BS}); 3) $\Omega_{HCHO\_BIRA}/\Omega_{NO2\_DP}$ (FNR_{OMI_BD}); 4) $\Omega_{HCHO\_SAO}/\Omega_{NO2\_DP}$ (FNR_{OMI_SD}). The combined relative uncertainty in FNR (σ_{FNR}/FNR) can be calculated as:

$$\frac{\sigma_{FNR}}{FNR} = \sqrt{(\frac{\sigma_{NO_2}}{\Omega_{NO_2}})^2 + (\frac{\sigma_{HCHO}}{\Omega_{HCHO}})^2 - 2(\frac{\sigma_{NO_2,HCHO}}{\Omega_{NO_2}\Omega_{HCHO}})} \quad (3)$$

where σ_{NO2} and σ_{HCHO} are the estimated individual errors for OMI NO_2 and HCHO, and $\sigma_{HCHO,NO2}$ is the covariance of these errors. Assuming a 20% relative uncertainty for OMI NO_2, a 30% relative uncertainty for OMI HCHO, and that the errors of the retrieved NO_2 and HCHO products are uncorrelated (i.e. $\sigma_{HCHO,NO2}$ =0), we estimate an overall FNR uncertainty of 36%. As the effects of clouds, aerosols, and albedo on satellite retrievals may cancel out, the uncertainty in FNR is expected to be lower than 36% [*Martin et al*., 2004a; *Duncan et al.*, 2010].

2.2 GEOS-Chem

We use the GEOS-Chem global 3D CTM (version 9.02; http://www.geos-chem.org) to simulate O_3-NO_x-CO-VOC-aerosol chemistry with 2° × 2.5 ° resolution for 2005 to 2012. These simulations are driven by Modern Era-Retrospective Analysis for Research and Applications (MERRA) meteorology [*Rienecker et al*., 2011]. Base anthropogenic emissions are from the Emission Database for Global Atmospheric Research (EDGAR) inventory for inorganic compounds [*Olivier et al*., 2007] and from the Reanalysis of the Tropospheric Chemical Composition (RETRO) inventory for organic compounds [*Schultz et al*., 2007], with regional overwrites for the United States (EPA National Emissions Inventory (NEI) 2005), Canada (National Pollutant Release Inventory), Mexico [*Kuhns et al*., 2005], Europe [*Auvray and Bey*, 2005], and South and East Asia [*Streets et al.*, 2006; *Zhang et al*., 2009]. Anthropogenic NO_x

emissions over the U.S.A., Canada, Japan and Europe are scaled each month based on estimates provided by the individual countries or regions [*van Donkelaar et al*., 2008]. The scale factors for North American are extended to 2012, and fixed after 2006 for other regions unless overwritten by regional emission inventories. No inter-annual scale factors are applied to anthropogenic VOCs. Additional inventories are applied for aircraft emissions [*Stettler et al*., 2011] and shipping [*Vinken et al.*, 2011]. Monthly biomass burning emissions are from the Global Fire Emissions Database version 3 [*van der Werf et al.*, 2010]. Biogenic VOC emissions follow the Model of Emissions of Gases and Aerosols from Nature scheme version 2.1 [*Guenther et al*., 2012]. Lightning NO_x emissions are as described by *Murray* [2016]. Soil microbial NO_x emissions are described by *Hudman et al.* [2012]. Monthly surface methane is prescribed from the NOAA GMD global surface network as a lower boundary condition [*Murray*, 2016]. Regional monthly average NO_x (including anthropogenic, natural and total) and VOC emissions (including anthropogenic, isoprene and total) are shown in Figure S1 and S2.

We sample model fields as one-hour averages between 1:00 and 2:00 pm local time (LT) to match the OMI overpass time. To examine the response of surface O_3 to precursor emissions, we conduct two perturbation simulations in GEOS-Chem that span 2006 to 2012, following a 12-month initialization period beginning in January 2005. First, we decrease global NO_x emissions by 20%. Second, we decrease global VOC emissions (including isoprene) by 20%. We calculate FNR_{GC} using the 3-D distribution of 1-2pm LT GEOS-Chem NO_2 and HCHO. We calculate the area-weighted average of all individual retrievals within each model grid cell. We sample modeled HCHO and NO_2 columns for the scenes concurrent with valid OMI observations to avoid sampling biases [*Boersma et al*., 2016]. To minimize random noise, we average both modeled and observed HCHO and NO_2 columns over seven days.

3 Evaluating space-based FNR as an indicator of surface O_3 sensitivity

In this section, we first evaluate the quantitative utility of FNR from a modeling perspective (Section 3.1), by correlating modeled column and surface FNR with the surface O_3 response to NO_x versus VOC emission reductions. We then examine the vertical profiles of HCHO and NO_2 in GEOS-Chem to better understand the spatial and temporal factors affecting column FNR relative to surface FNR (Section 3.2). Section 3.3 compares seven-day average OMI FNR with that simulated from GEOS-Chem.

3.1 Relating FNR to surface O_3 sensitivity

Previous studies characterize the transition between NO_x-sensitive and NO_x-saturated ozone production in different ways, such as the response of surface O_3 to emission perturbations [e.g. *Martin et al.*, 2004a], correlations between O_3 and NO_y or NO_z [e.g. *Jacob et al*., 1995], or radical loss pathways [e.g. *Kleinman et al.*, 1994; *Duncan et al*., 2010]. Different methods may identify different threshold values marking the transition between chemical production regimes. Figure 1 shows the normalized surface O_3 responses to the perturbed NO_x and VOC emissions change (i.e. $d[O_3]/dE$) in GEOS-Chem versus the surface and column FNR averaged between 1 to 2 PM for all polluted model grid cells within our three regions (grid cells where multi-year average $\Omega_{NO2\_GC} > 2.5 \times 10^{15}$ molecules/cm^2). In general, the surface O_3 response to NO_x emission reductions increases with FNR, and the surface O_3 response to VOC emission reductions decreases with surface FNR. We define negative $d[O_3]/dE_{NOx}$ as NO_x-saturated (VOC-limited) conditions. In this chemical regime, reductions in NO_x emissions increase surface O_3 due to NO titration effects and reductions in VOC emissions decrease surface O_3. NO_x-limited conditions occur when the surface O_3 response to NO_x emission reductions is larger than that to VOC emission reductions (i.e. $d[O_3]/dE_{NOx} > d[O_3]/dE_{VOC}$). We refer to the intermediary conditions as a mixed or "transitional" regime.

Spatial variations in meteorological and photochemical conditions, as well as in downwind transport of ozone produced in upwind grid cells, can produce a range of $d[O_3]/dE_{NOx}$ sensitivities for any given FNR value (Figure 1). Despite these variations, surface FNR can qualitatively distinguish between NO_x-saturated and NO_x-limited conditions (Figure 1). The majority (90%) of NO_x-saturated grid cells are associated with surface FNR < 0.6; over 90% of NO_x-limited conditions are associated with surface FNR > 0.9. In the model, the surface FNR values thus mark a clear separation between the NO_x-saturated and NO_x-limited regimes. Figure 2 shows the cumulative probability of correctly identifying the NO_x-limited or the NO_x-saturated regime at a given FNR value in the GEOS-Chem model. The intersection of the two lines marks the point at which the probability of identifying NO_x-limited and NO_x-saturated correctly is equal. This intersection occurs around 0.65 for North America, 0.5 for Europe and 0.7 for East Asia (Figure 2). Below this value, the likelihood of correctly identifying NO_x-limited conditions increases, while the likelihood of identifying NO_x-saturated conditions decreases.

Instead of defining a single cut-off value between NO_x-saturated and NO_x-limited conditions, we define a range of values marking a "transitional regime" to lower the probability of misclassification (i.e. incorrectly classifying NO_x-saturated as NO_x-limited or vice versa). A wider transitional regime lowers the chance of misclassification but generates more grid cells where ozone sensitivity is regarded as mixed or uncertain. If the regime threshold values are set between 0.5 and 0.8 for North America so that the probability of misclassification is 5%, then 10% of NO_x-saturated and 5% of NO_x-limited conditions will be incorrectly considered as transitional. If we widen the transitional regime to lower the probability of misclassification to 2%, ~50% of NO_x-saturated and ~10% of NO_x-limited conditions will instead be classified as transitional (Figure 2). We define the regime threshold values as those where the cumulative probability of NO_x-saturated and NO_x-limited conditions is 95% (i.e. the probability of misclassification is 5%) that reflect a balance between accuracy and certainty.

Next, we investigate whether the above regime definition should be applied to derive the regime threshold values globally, regionally or individually for each grid cell. Combining all data over the polluted areas of the three regions, we find the transition regime occurs between values for surface FNR of 0.4 and 0.7 (Figure 2). Separating by region, we find that the regime transition occurs between smaller surface FNR values for Europe (0.4 ~ 0.6) than over North America and East Asia (0.5 ~ 0.8) (Figure 2). Figures 3 (a) to (c) shows the classification accuracy (percentage of correct classifications of NO_x-saturated or NO_x-limited conditions) when we apply the regionally-derived range of values for the transition regime. The overall accuracy is high (> 90%) over the majority of polluted areas in the three regions. Lower accuracy is found over California (82%), England (~75%), and North East China (~80%), regions with high anthropogenic emission regions. The high accuracy implies that surface FNR is a quantitatively robust metric for diagnosing the response of surface O_3 to changes in VOC and NO_x emissions.

If we instead derive the regime threshold values separately in each model grid cell, we obtain spatially varying values marking the boundaries of the transitional regime, with higher threshold values over low-latitude regions. This approach, however, does not always improve the accuracy (Figure 3 (d) to (f)), which decreases over California (< 70%), Northeast U.S.A. (< 70%), England (< 70%), the Netherlands (< 60%) and North East China (40% ~ 70%). The low accuracy over these regions reflects a less pronounced correlation between FNR and $d[O_3]/dE$,

and therefore the derived regime threshold values are less stable. Our approach assumes changes in $[O_3]$ in each grid cell are due to the emissions within that box, but $[O_3]$ is also influenced by pollution transported from upwind regions, which could also account for the low accuracy. *Sillman et al.* [2002] suggests the indicator ratios behave differently for rural and urban environment. The global model resolution cannot fully capture these urban-rural gradients, and therefore even the pixel-based derivation of values marking regime thresholds is unable to characterize fine-scale variations of the photochemical environment. We thus conclude that the regionally-based regime threshold values are most appropriate for surface FNR if a global model is applied to derive the regime threshold. Despite spatial and temporal differences in the factors affecting O_3 production (abundance of solar radiation, VOCs, NO_x and VOC speciation), surface FNR can identify the large-scale variation of O_3 sensitivity.

While the column FNR is also able to separate the NO_x-saturated and NO_x-limited conditions qualitatively, modeled column FNR correlates less significantly with surface O_3-NO_x-VOC sensitivity compared to surface FNR. While $d[O_3]/dE_{NOx}$ tends to be negative at low column FNR, and positive at high column FNR (Figures 1(b)), negative $d[O_3]/dE_{NOx}$ still occurs for some high values of column FNR. Nevertheless, the column FNR values marking the boundary between NO_x-saturated and transitional regimes are 0.9 for all three regions (Figure 2). The boundary between the transitional and NO_x-limited regimes, however, varies: 1.4 for North America, 1.2 for Europe and 1.6 for East Asia (Figure 2). *Martin et al.* [2004a] previously identified a column FNR value of 1 to separate NO_x-limited and NO_x-saturated regimes (Table 1) using GEOS-Chem (version 4.16), close to the threshold value of 0.9 that we find for North America. *Duncan et al.* [2010] estimated that this regime transition occurs across a column FNR range of 1 - 2 (Table 1) over California. They diagnosed this value as when the radical loss rate through HO_x equals that lost through NO_x ($L_{HOx}/L_{NOx} = 1$). Using column FNR to classify the O_3 sensitivity degrades accuracy across all three regions (Figure 3 (d) to (f)) by about 10% compared to surface FNR. Using spatially varying regime threshold values improves the classification accuracy over most area, suggesting that spatially-varying regime threshold values may be more suitable for column FNR, but the accuracy is still low over those low-accuracy regions identified from surface FNR.

3.2 Column-to-surface relationship

We find that the surface and column indicators are robust, providing confidence in the utility of FNR to represent photochemical conditions relevant to ozone production. We address here the uncertainty as to whether the ratio of the vertically integrated column represents the near-surface environment. That is, the relationship of surface to column FNR varies spatially and temporally, mainly due to differences in vertical profiles of NO_2 and HCHO. As in previous studies, we use a model (GEOS-Chem) to adjust column-based ratios observed from satellite instruments to surface-based ratios that are more relevant to near-surface ozone formation [*Lamsal et al.*, 2008; *Zhu et al.*, 2017]. To relate the column-based and surface-based indicator ratios, we calculate the ratio of the GEOS-Chem simulated tropospheric column densities to near-surface number densities of NO_2 and HCHO, defined as an effective boundary layer height for each species (BLH_{eff_NO2} and BLH_{eff_HCHO}) [*Halla et al.*, 2011]:

$$BLH_{\text{eff}} = \frac{\Omega_x}{N} \quad (4)$$

where Ω_x is the model simulated tropospheric vertical column density of species x (molecules/cm^2), and N is the model simulated number density of species x of the surface layer (molecules/cm^3). Similarly, the conversion factor (f_{c_s}) between column and surface FNR is calculated as the ratio of column FNR to surface FNR, which is equivalent to the ratio of BLH_{eff_HCHO} to BLH_{eff_NO2}. Generally, if NO_2 or HCHO is well mixed within a homogeneous boundary layer, and most NO_2 or HCHO exists in the boundary layer, the effective boundary layer height should approximate the meteorological boundary layer height [*Halla et al.*, 2011]. As such, it is expected that the column-to-surface relationship of trace gases depends on the PBL height.

Figure 4 shows the relationships between daily meteorological PBLH and BLH_{eff_NO2} and BLH_{eff_HCHO} aggregated over polluted grid cells of the three regions from 2005 to 2012. BLH_{eff_NO2} is correlates strongly with PBLH (R = 0.85), as expected for a short-lived species emitted mainly at the surface. BLH_{eff_NO2} is higher than the simulated PBLH, implying a non-negligible contribution of free tropospheric NO_2 to the total tropospheric column density (such as from lightning NO_x [*Travis et al.*, 2016; Figure S5]). In contrast, there is little to no relationship of the HCHO vertical profile to PBLH (R = 0.01). HCHO is a secondary photochemical product,

formed throughout the atmosphere, with a smaller vertical gradient NO_2, leading to smaller fraction of HCHO within the boundary layer than for NO_2 (Figure 5). The vertical gradient of HCHO is larger in warm season than cold season due to larger contribution of isoprene as a source of HCHO, while the vertical gradient of NO_2 is smaller in warm season (Figure 5) when the surface emission generally mixes through deeper boundary layer and the lightning NO_x source and deep convective mixing are most active. These differences between the NO_2 and HCHO vertical distributions affect the surface and column FNR, and can be accounted for by adjusting the values marking the boundaries of the transitional regime to reflect seasonal and spatial variations in the relationship between column FNR and surface photochemical conditions. As shown in Figure 4 (c), f_{c_s} is inversely correlated with PBLH (R = 0.78), largely driven by the PBLH dependence of NO_2 (Figure 4 (a)).

The spatial variation of f_{c_s} implies that column-based FNR shows less spatial variability than surface-based FNR (Figure S4). BLH_{eff_NO2} varies seasonally by a factor of 2 yet BLH_{eff_HCHO} varies little, with winter-summer differences of less than 500 m. Figure 6 shows a clear seasonal cycle of f_{c_s} over polluted areas in North America and Europe, with a December maximum and July minimum. The shapes of the seasonal cycles of f_{c_s} oppose those of column FNR (Figure 7), which implies that column-based FNR tends to dampen the seasonality of surface FNR. Both Europe and North America show larger seasonal cycles than East Asia, where f_{c_s} in January exceeds that of July by a factor of 3. The seasonal cycle of BLH_{eff_HCHO} in East Asia correlates with PBLH and BLH_{eff_NO2}, with maxima in spring and fall (Figure S5), yielding a smaller f_{c_s} seasonal cycle.

As the relationship between surface and column FNR varies spatially and temporally (section 3.1), we adjust the column-based FNR values marking the transitional ozone production regime by applying the modeled f_{c_s} to the threshold values of surface FNR. The variation in column-to-surface relationships of NO_2 and HCHO is dependent on the vertical profiles, which are mostly driven by meteorology. We find the column-to-surface relationship of FNR does not vary much year-to-year: the standard deviation for any given month is lower than 8% for all regions (Figure S6). We find no statistically significant trends in the column-to-surface relationships, suggesting that the constant regime threshold values will not affect the trend analysis in Section 4. Also, as we are attempting to generalize the derived regime threshold

values for application beyond the model simulation period, constant regime threshold values are preferred. Therefore, we do not adjust the regime threshold values to include inter-annual variability of the column-to-surface relationships. The pink band in Figure 7 shows the seasonal cycle of these model-simulated column-based values averaged from daily data within each month over the polluted regions separately within North America, Europe and East Asia. The lighter band represents the 1σ deviation of these values derived from individual polluted grid cells in each regional domain. Larger standard deviations occur over Europe, reflecting stronger spatial variations of the column FNR values spanning the transitional regime. The coarse spatial resolution of GEOS-Chem cannot capture sharp urban-rural gradients though it does resolve large-scale variations in meteorology and topography. The maximum standard deviation occurs in spring, when meteorological conditions range widely during the transition from winter to summer and the onset of biogenic emissions.

Following the seasonal cycle of the column-to-surface relationship (Figure 6), the transitional regime thresholds in Figure 7 are higher in the cold season than in the warm season. The transition from the NO_x-saturated to the transitional regime occurs for column-based FNR ranging from 0.5 in June to 1.6 in January over North America, 0.8 in June to 1.0 in January over East Asia, and 0.6 in August to 1.8 in January over Europe. The thresholds between the transitional and the NO_x-limited regime range from 0.8 in July to 2.5 in December for North America, 1.2 in August to 1.6 in December for East Asia, and 0.9 in July to 2.7 in December for Europe. East Asia shows a smaller seasonal cycle in these threshold values compared to North America and Europe. The threshold from NO_x-saturated to transitional regime is generally smaller than 1.0 as proposed in *Duncan et al.* [2010], likely due to different definitions for the transitional regime (Table 1).

3.3 Model and satellite comparison

While the model demonstrates that tropospheric column ratios of HCHO to NO_2 can indicate surface O_3 sensitivity to NO_x and VOC emissions, both satellite retrievals and model simulations are subject to large uncertainties. Here we compare the OMI-derived seven-day average FNR with the GEOS-Chem base-case simulation to identify where and when the satellite products and model agree best, implying more confidence in our understanding. We restrict the comparison to polluted regions, defined as those grid cells in GEOS-Chem where annual average

tropospheric $\Omega_{NO2\_GC} > 2.5\times10^{15}$ molecules/cm^2. Table 2 summarizes the comparison between modeled and OMI FNR.

We find that the correlation coefficient between the model- and satellite-derived FNR products depends on the choice of NO_2 product, while the mean bias depends on the choice of HCHO product. FNR_{OMI} (with GEOS-Chem profiles applied) using Ω_{NO2_SP} (R: 0.44 ~ 0.74) correlates better with GEOS-Chem than Ω_{NO2_DP} (R: 0.28 ~ 0.63) for all three regions. Among the four combinations, FNR_{OMI_SS} correlates best with FNR_{GC} over North America and East Asia, while FNR_{OMI_BS} correlates best over Europe. The choice of HCHO product does not influence the overall correlation, except over Europe where using Ω_{HCHO_BIRA} results in a higher correlation coefficient compared to Ω_{HCHO_SAO}. The low correlation coefficient of FNR_{OMI_SD} and FNR_{OMI_BD} is largely caused by observations with low Ω_{NO2_SP} and Ω_{NO2_DP} over clean regions ($\Omega_{NO2} < 1.5\times10^{15}$ molecules/cm^2). We find both Ω_{NO2_DP} and Ω_{NO2_SP} match Ω_{NO2_GC} over polluted regions, and the mean differences with GEOS-Chem are within 5% for both products (Table S1). FNR_{OMI} is on average higher than FNR_{GC} by 10% to 40% if Ω_{HCHO_BIRA} is used, and lower than FNR_{GC} by 10% to 30% using Ω_{HCHO_SAO}. The opposite sign of the mean offset results from the large difference between two HCHO retrievals: Ω_{HCHO_SAO} is on average 50% lower than Ω_{HCHO_BIRA} across the three regions (Table S1). Discarding observations with negative HCHO columns corrects the negative offsets of FNR_{OMI_SS} and FNR_{OMI_SD} relative to the model, but increases the positive offsets of FNR_{OMI_BD} and FNR_{OMI_BS}.

Although the absolute values of FNR_{OMI} differ from FNR_{GC}, FNR_{OMI} is in general able to capture the spatial and temporal variation of the O_3 production regime inferred from FNR_{GC}. The agreement (defined as the percentage of both FNR_{GC} and FNR_{OMI} falling in the same photochemical regime) is higher than 80% for warm season and 60% for cold season across three regions (Table 2). The agreement also depends on the choice of HCHO product, especially in warm season. Figure 7 shows the seasonal cycle of FNR_{GC} and FNR_{OMI} averaged from 2005 to 2012 for each region. FNR_{OMI} shows a positive offset and low correlation coefficient in cold season for all four combinations, especially over Europe, reflecting the HCHO overestimate in winter. Nevertheless, the products and model all agree that NO_x-saturated or transitional regimes dominate in winter. FNR_{GC}, along with the four combinations of OMI observed FNR, indicate

468 NO_x-limited regimes from May to September over all three regions, but may disagree for
469 individual grid cells (Figure S7 to S10). FNR_{GC} disagrees with FNR_{OMI} more frequently in spring
470 and fall during the transitions between regimes. FNR_{OMI_BD} and FNR_{OMI_BS} are consistently
471 higher than FNR_{GC} over all three regions, leading to a longer NO_x-limited regime versus FNR_{GC},
472 but they match regimes diagnosed with FNR_{GC} better in warm season (Table 2). In contrast,
473 FNR_{OMI_SS} and FNR_{OMI_SD} are lower than FNR_{GC}, especially in the warm season, leading to a
474 longer NO_x-saturated and transitional regime, and better match the ozone production regimes
475 indicated by FNR_{GC} in cold season (Table 2).

476 The re-gridded FNR_{OMI} at coarse resolution tends to smear spatial gradients in ozone
477 production regimes. To characterize the spatial heterogeneity of O_3 sensitivity to its precursor
478 emissions, we recommend the Level-3 OMI HCHO and NO_2 data available at 0.25° × 0.25° for
479 general applications of the indicator ratio that do not involve comparison or interpretation with a
480 model. We compare FNR_{GC} with Level-3 FNR_{OMI_BS} ($FNR_{OMI\_BS\_L3}$) by spatially matching
481 Level-3 data to the model grid. Using different prior profile shapes leads to minor differences in
482 AMFs for NO_2 and HCHO (Table S1). While model-satellite discrepancies are larger for
483 $FNR_{OMI\_BS\_L3}$ *vs.* FNR_{OMI_BS} derived with our daily GEOS-Chem profiles, the overall correlation
484 is comparable to and even better than FNR_{OMI_BD} and FNR_{OMI_SD} over Europe and East Asia
485 (Table 2). $FNR_{OMI\_BS\_L3}$ is on average higher than FNR_{GC} by 20%. Evaluation with aircraft data
486 suggests GEOS-Chem underestimates HCHO concentrations by 10% over the southeast U.S.A.
487 [*Zhu et al.*, 2016]. In order to correct this systematic model-satellite discrepancy, which likely
488 reflects the model underestimate of HCHO, we additionally correct the regime thresholds for
489 $FNR_{OMI\_BS\_L3}$ by increasing the values marking the boundaries of the transitional regimes
490 derived from section 3.2 by 20%.

491 **4 Decadal changes of O_3-NO_x-VOC sensitivity**

492 Here we investigate the decadal trend of surface O_3 sensitivity over polluted areas in
493 North America, Europe, and East Asia. For this application, we use monthly average Level-3
494 gridded with the original standard AMFs included in the products from 2005 to 2015 [*Duncan et*
495 *al.*, 2010; *Jin and Holloway*, 2015]. Satellite-derived ozone production regimes generally agree
496 with *in-situ* ground-based studies over the three regions (Table 3), but OMI observations tend to
497 overestimate the NO_x sensitivity. The OMI overpass time is in the afternoon, when the NO_2 level

498 is at its daily minimum and thus ozone production is most NO_x-limited. The horizontal resolution
499 of OMI data is likely to miss urban core NO_x-saturated regimes sampled at individual urban sites
500 (e.g. *Pusede et al*., [2012]).

501 Before applying the OMI L3 product to analyze decadal trends, we investigate whether
502 long-term changes in FNR are compromised by instrument degradation and data availability
503 changes. First, *Marais et al.* [2012] suggest an artificial increase in the background HCHO
504 column in the OMI SAO retrieval due to instrument degradation. This feature does not appear in
505 the BIRA retrieval, which applies a zonal reference sector correction (e.g., Figure S11).
506 $FNR_{OMI\_BS\_L3}$ does not show any artificial trend over remote Pacific region either (Figure S11).
507 Second, OMI data coverage has decreased over the years mostly due to growing row anomalies
508 (Figure S12), which tend to decrease monthly average HCHO column with time [*De Smedt et al*.
509 2015]. We find that the data coverage has declined by about 20% from 2005 to 2015 for both the
510 Level-3 OMI HCHO and NO_2 products, implying that these sampling biases may largely cancel
511 out when we take the HCHO/NO_2 ratio (Figure S12). To test the influence of this sampling bias,
512 we calculate another time series of monthly average FNR that randomly discards the
513 corresponding number of daily HCHO and NO_2 data such that that the data coverage for a given
514 month is set as the minimum number of samples obtained during that month between 2005 and
515 2015 (Figure S13). There is no systematic offset due to the changing data coverage. We find that
516 sampling differences may influence the magnitude of the FNR_{OMI} trend (slope), but have little
517 impact on the diagnosed changes in the ozone production regimes (Figure S13 versus Figures 8 -
518 11). Note that our definition of regimes relies on the modeled values that do not include inter-
519 annual variability (pink shaded bands in Figure S13), and therefore the changes over time in the
520 ratio reflect trends in the satellite products that do not contain any information from model. It
521 should also be noted that a higher solar zenith angle cut-off was applied to the HCHO retrieval
522 mainly reflecting the lower retrieval sensitivity to HCHO as compared to NO_2. The data
523 coverage of satellite-derived HCHO is thus smaller than for NO_2. We calculate a new time series
524 of monthly average FNR that is constructed using only days when both HCHO and NO_2 have
525 valid data. We find similar trends in FNR and in changes in the ozone production regime (Figure
526 S14) as for our original time series that includes all available data (Figures 8 - 11), but the

resampled data show larger fluctuations, due to increasing uncertainties as the number of observations used for temporal averaging decreases.

4.1 North America

From 2005 to 2015, NO_x sensitivity increased over populated regions of North America (Figures 8 and 9). Previous studies have shown that NO_2 levels decreased by 25% to 55% over the continental U.S.A. over the past decade, resulting from the implementation of nationwide emission controls [*Lamsal et al.*, 2015; *Schneider et al.*, 2015; *Tong et al.*, 2015; *Duncan et al.*, 2016]. *De Smedt et al.* [2015] note a decreasing trend of HCHO (-10% to -2%) over the eastern U.S.A. and California from 2005 to 2014, but the magnitude is much less significant than NO_2, as the main source of HCHO from biogenic emissions fluctuates with meteorology [*Guenther et al.*, 2006; *Millet et al.*, 2008]. The NO_x-limited regime dominates over the northeast U.S.A. in both May 2005 and 2015. The $FNR_{OMI\_BS\_L3}$ indicates New York City was in NO_x-saturated regime in May 2005, but shifted to NO_x-limited by 2015. The NO_x-limited regime occurred from June to August in NYC in 2005, and the length of the NO_x-limited regime increased from three months in 2005 to five months in 2015 (Figure 8). The average length of the NO_x-limited regime in 2005 to 2009 is 3.2 months, and increases to 4.2 months for the 2011 to 2015 period. The length of the NO_x-saturated regime has decreased from eight months in 2005 to five months in 2015. The five-year average length of the NO_x-saturated regime has decreased from 7.4 (2005 to 2009) to 6.0 months (2011 to 2015). Over Chicago, $FNR_{OMI\_BS\_L3}$ varies inter-annually but increases by 0.10 per year from 2005 to 2015, extending the average length of NO_x-limited regime from 3.0 months between 2005 to 2009 to 4.8 months between 2011 and 2015, and narrowing the NO_x-saturated regime from 7.2 to 5.2 months. *Jing et al*. [2014] suggest O_3 formation has shifted from NO_x-limited to VOC-limited in 2008/2009, but such increasing VOC sensitivity is not observed from $FNR_{OMI\_BS\_L3}$. We also find similar regime shifts in other cities such as Detroit and Los Angeles (not shown). For other cities with pronounced emission reductions [*Duncan et al.*, 2016], such as Philadelphia, Atlanta and Phoenix, while the O_3 production regime remains NO_x-limited in the warm season, we find an increasing trend of $FNR_{OMI\_BS\_L3}$ and consequently enhanced NO_x sensitivity (not shown). The observed increasing NO_x sensitivity over the U.S. cities implies that continued regional NO_x emission control

programs should be effective for surface O_3 mitigation, as shown in modeling studies [*Frost et al.*, 2006; *Song et al.*, 2010].

4.2 Europe

Similar to U.S. cities, surface O_3 production is becoming more sensitive to NO_x (NO_x-limited) over Europe in response to decreasing NO_x emissions. Satellite-derived NO_2 products also show significant decreasing trends of -50% to -3% over Europe and Russia, driven by a combination of environmental policy and reduced economic activity during recessions [*Castellanos and Boersma*, 2012; *Duncan et al.*, 2016]. No significant HCHO trend occurs over Europe [*De Smedt et al.*, 2015]. We find that transitional and NO_x-saturated regimes were dominant over Great Britain and western Europe in July 2005. Ozone production regimes transitioned to NO_x-limited regime in northern England, Germany and France in 2015 (Figure 10). Overall, an increasing trend of $FNR_{OMI\_BS\_L3}$ occurs over London, extending the average length of the NO_x-limited regime from 1.4 months between 2005 and 2009 to 2.4 months between 2011 and 2015. The five-year average length of Surface O_3 production in London was sensitive to VOC emissions most of the year between 2005 and 2014 except for July 2009 when $FNR_{OMI\_BS\_L3}$ reached the NO_x-limited regime. We find a sharp increase of $FNR_{OMI\_BS\_L3}$ in 2015, with surface O_3 production NO_x-limited in July and August. Amsterdam also shows an increasing trend of $FNR_{OMI\_BS\_L3}$ that peaks in 2012, and the length of NO_x-limited regime has increased from 2.0 (2005 to 2009) to 2.8 months (2011 to 2015). Note the average $FNR_{OMI\_BS\_L3}$ was relatively low in urban areas of Europe compared with cities in North America with similar of NO_x emission levels. This may reflect low HCHO concentration in Europe due to lower biogenic emissions [*De Smedt et al.*, 2015]. As shown in Figure 10, monthly average $FNR_{OMI\_BS\_L3}$ over London and Amsterdam does not vary significantly with season from 2005 to 2015. This finding, however, does not necessarily indicate a weak seasonality of O_3 sensitivity. f_{c_s} varies with season by a factor of three over Europe (Figure 6), which dampens the seasonal cycle of the column-based $FNR_{OMI\_BS\_L3}$. Also, OMI observations of HCHO and NO_2 at high latitudes are subject to large uncertainties due to signal interference of unknown species [*González Abad et al.*, 2015]. Most wintertime observations were excluded due to high solar zenith angle and larger retrieval uncertainty.

4.3 East Asia

The trends in surface O_3-NO_x-VOC sensitivity are uneven and mixed over East Asia, where we find increasing NO_x sensitivity over Japan and Korea, and an overall increasing VOC sensitivity over China (Figure 11). Changes in surface O_3 sensitivity over China have been investigated in *Jin and Holloway* [2015] using OMI observations under the assumption of that the transitional regime occurs when 1<FNR<2. This study builds upon *Jin and Holloway* [2015] by incorporating the seasonality of column-to-surface relationships when defining the transitional regime. We find here that the transition to the NO_x-limited regime in summer occurs at $FNR_{OMI\_BS\_L3} < 2$, and the transition to the NO_x-saturated regime occurs at $FNR_{OMI\_BS\_L3} < 1$, leading to a larger spatial extent of the NO_x-limited regime in summer and the NO_x-saturated regime in winter compared to *Jin and Holloway* [2015]. *Jin and Holloway* [2015] show a spatial and temporal expansion of the NO_x-saturated regime over East China, but the developed megacities, such as Beijing, Shanghai and Guangzhou, show an increasing NO_x sensitivity due to NO_x emission reduction. The duration of NO_x-limited regime extended from one month in 2005 to four months in 2015 over Beijing (Figure 11). The average length of the NO_x-limited regime from 2005 to 2009 is 1.4 months, and increased to 2.2 months from 2011 to 2015. However, the length of NO_x-saturated regime remains around 8 months throughout the entire period from 2005 to 2015. $FNR_{OMI\_BS\_L3}$ increased sharply in the summer of 2008, reflecting emission controls during the Beijing Olympic Games [*Wang et al.*, 2009]. For other cities over the Northern China Plain such as Jinan (Figure 11(b)), O_3 production regimes in May have become NO_x-saturated since 2011. $FNR_{OMI\_BS\_L3}$ in Jinan decreased from 2005 to 2011, and remained stable since 2011, likely associated with nationwide NO_x reductions from power plants [*Liu et al.*, 2016]. The length of NO_x-saturated regime has increased from eight months between 2005 and 2009 to nine months between 2011 and 2015. The Pearl River Delta shows increasing NO_x sensitivity due to successful NO_x emission control; O_3 sensitivity was in the transitional regime in May 2005, but shifted to the NO_x-limited regime in 2015. *Duncan et al.* [2016] found large decreases of OMI NO_2 levels over South Korea and Japan, attributed to national environmental regulations. We find an increasing NO_x sensitivity over Korea and Japan accordingly. Seoul and Tokyo were in the NO_x-saturated regime in May 2005, and they both shifted to the transitional regime in 2015 (Figure 11). The value of $FNR_{OMI\_BS\_L3}$ was consistently below the upper boundary of transitional regime in Tokyo (Figure 11(c)) and Seoul (Figure 11(d)), where surface O_3

616 production was either NO_x-saturated or transitional except for July 2015 in Seoul and August
617 2015 in Tokyo. *Duncan et al.* [2016] suggest that effective domestic control strategies may have
618 been negatively offset by increasing trans-boundary NO_x emissions from China, resulting in a
619 smaller positive trend in $FNR_{OMI\_BS\_L3}$ in Seoul and Tokyo than over European and U.S cities
620 with similar emission changes.

621 **5 Conclusions**

622 We use OMI observations of NO_2 and HCHO column densities, along with a global
623 chemical transport model (GEOS-Chem) to examine the sensitivities of surface O_3 pollution to
624 NO_x and VOC emissions over northern mid-latitude source regions. We use the GEOS-Chem
625 model to determine the regime thresholds for FNR with two emission perturbation simulations.
626 We find that surface FNR in the model does indicate surface O_3 sensitivity, and that regionally
627 constant FNR thresholds can separate the NO_x-limited and NO_x-saturated conditions to at least
628 90% confidence. FNR values marking the boundaries of the photochemical regimes are derived
629 from the model, and thus depend on the mechanism used to represent photochemistry. *Travis et*
630 *al.* [2016] suggest an overestimate of NO_x emissions over the eastern U.S.A. Such an
631 overestimate could lead to excessive tropospheric NO_2 columns as well as an underestimate of
632 $d[O_3]/dE_{NOx}$, which may largely cancel out so that the threshold values would be less sensitive to
633 this error. Erroneously high NO_2 columns, however, could lead us to diagnose excessively low
634 regime threshold values over NO_x-saturated regions.

635 Column FNR shows a lower regime classification accuracy, largely due to variations in
636 column-to-surface relationships. The column-to-surface relationships for NO_2 correlate strongly
637 with PBLH, but weakly for HCHO. As a result, the column-to-surface relationship of FNR (f_{c_s})
638 is inversely correlated with PBLH. Following the spatial and temporal variations of PBHL, f_{c_s}
639 shows pronounced seasonal cycles with maxima in winter and minima in summer, which act to
640 dampen the spatial and temporal variation of surface O_3 sensitivity. We adjust the regime
641 threshold values for column-based FNR using the modeled f_{c_s}. The derived column FNR
642 thresholds marking the boundaries between ozone production regimes vary by a factor of 3 over
643 North America and Europe. The modeled vertical profiles are also sensitive to the PBL scheme.
644 Full PBL mixing scheme is implemented in GEOS-Chem. The full-mixing scheme in GEOS-

Chem is likely to underestimate the vertical gradient of both NO_2 and HCHO [*Lin et al*., 2010; *Zhang et al.*, 2016].

Even though modeled FNR can indicate surface O_3 sensitivity to NO_x vs. VOC precursors, both satellite-derived and modeled FNR are subject to uncertainties. We compare four combinations of two OMI HCHO products (BIRA, SAO) and OMI NO_2 (DP, SP) products with GEOS-Chem simulations. The spatial and temporal correlation between the modeled and observed indicator ratios depends on the choice of NO_2 product, while the mean bias depends on the choice of HCHO product. We note that wintertime satellite retrievals of HCHO incur large uncertainties due to diminished satellite sensitivity near the surface [*De Smedt et al.,* 2015]. Qualitatively, however, such uncertainties should not affect the conclusion that ozone production is NO_x-saturated in winter over regions heavily influenced by anthropogenic emissions, as noted in previous studies [*Kleinman*, 1991, 1994; *Jacob et al.*, 1995]. Satellite-derived O_3 sensitivity generally agree with *in situ* observations performed in previous studies. While the distinct behavior of indicator ratio over urban and rural environment cannot be fully resolved from the coarse resolution of global model, the finer resolution of OMI observation can explain the majority of the spatial and temporal variation of O_3 sensitivity. Future work could assess the ability of the OMI indicator ratio to reveal urban fine-scale features with a higher resolution (e.g., regional) model.

Combining model-derived threshold values with a decadal record of satellite observations, we further investigate how O_3 production sensitivity to precursors has changed over the 2005 to 2015 period. We find a general increase in FNR_{OMI} over the urban areas of North America, Europe, South Korea and Japan from 2005 to 2015, driven by NO_x emission reductions imposed over the past decade. The spring transition to a NO_x-limited regime has shifted earlier in some megacities, and the NO_x-limited regime has become dominant in summer. China shows an overall decrease in FNR_{OMI} except for the most developed areas such as Beijing, Shanghai and Pearl River Delta, where emission control strategies have been implemented. In our FNR analysis, HCHO serves as an indicator of reactivity-weighed VOCs, but the yield and production of HCHO from isoprene is non-linearly dependent on the NO_x level [*Wolfe et al*., 2016]; this non-linearity implies that FNR may underestimate increases in NO_x sensitivity as NO_x emissions decline.

Surface O_3 sensitivity also varies throughout the day and from day to day. The suitability of the FNR_{OMI} for daily variation is still limited by the uncertainties associated with the OMI HCHO and NO_2 retrievals. In addition, the spatial resolution of OMI may be too coarse to reveal VOC-limited chemistry in urban cores. Near-term advances in space-based observations of HCHO and NO_2 from geostationary satellites as anticipated to occur over East Asia (Geostationary Environment Monitoring Spectrometer), Europe (Sentinel-4) and North America (Tropospheric Emissions: Monitoring of Pollution) [*Lahoz et al.*, 2012], offer exciting opportunities to explore the potential for space-based FNR to diagnose ozone production regimes at finer spatial and temporal scales.

Acknowledgements:

Support for this project was provided in part by the NASA Air Quality Applied Sciences Team (AQAST, Grant NNX12AF15G), NASA Atmospheric Composition Modeling and Analysis Program (ACMAP, Grant NNX17AG40G), and NASA Health and Air Quality Applied Sciences Team (HAQAST, Grant NNX16AQ20G). The NASA OMI NO_2 and HCHO data are publicly available from the NASA Goddard Earth Sciences Data Active Archive Center (GES DISC; http://disc.sci.gsfc.nasa.gov). We acknowledge the free use of the OMI BIRA-IASB HCHO and DOMINO NO_2 products from the Tropospheric Emission Monitoring Internet Service (TEMIS; http://www.temis.nl).

Disclaimer:

The research described in this article has been reviewed by the National Exposure Research Laboratory, US Environmental Protection Agency and approved for publication. Approval does not signify that the contents necessarily reflect the views and the policies of the Agency nor does mention of trade names or commercial products constitute endorsement or recommendation for use.

References:

Auvray, M. and I. Bey (2005), Long-range transport to Europe: Seasonal variations and implications for the European ozone budget, *J. Geophys. Res.*, *110*(D11), D11303–22, doi:10.1029/2004JD005503.

Boeke, N. L. et al. (2011), Formaldehyde columns from the Ozone Monitoring Instrument: Urban versus background levels and evaluation using aircraft data and a global model, *J. Geophys. Res.*, *116*(D5), D05303, doi:10.1029/2010JD014870.

Boersma, K. F. et al. (2011), An improved tropospheric NO_2 column retrieval algorithm for the Ozone Monitoring Instrument, *Atmos. Meas. Tech.*, *4*(9), 1905–1928, doi:10.5194/amt-4-1905-2011.

Boersma, K. F., G. C. M. Vinken, and H. J. Eskes (2016), Representativeness errors in comparing chemistry transport and chemistry climate models with satellite UV–Vis tropospheric column retrievals, *Geosci. Model Dev.*, *9*(2), 875–898, doi:10.5194/gmd-9-875-2016.

Boersma, K. F., H. J. Eskes, and E. J. Brinksma (2004), Error analysis for tropospheric NO_2 retrieval from space, *Journal of Geophysical Research: Atmospheres (1984–2012)*, *109*(D4), doi:10.1029/2003JD003962.

Bucsela, E. J., N. A. Krotkov, E. A. Celarier, L. N. Lamsal, W. H. Swartz, P. K. Bhartia, K. F. Boersma, J. P. Veefkind, J. F. Gleason, and K. E. Pickering (2013), A new stratospheric and tropospheric NO_2 retrieval algorithm for nadir-viewing satellite instruments: applications to OMI, *Atmos. Meas. Tech.*, *6*(10), 2607–2626, doi:10.5194/amt-6-2607-2013.

Campbell, P. et al. (2015), A multi-model assessment for the 2006 and 2010 simulations under the Air Quality Model Evaluation International Initiative (AQMEII) phase 2 over North America: Part I. Indicators of the sensitivity of O_3 and $PM_{2.5}$ formation regimes, *Atmospheric Environment*, *115*(C), 569–586, doi:10.1016/j.atmosenv.2014.12.026.

Castellanos, P., and K. F. Boersma (2012), Reductions in nitrogen oxides over Europe driven by environmental policy and economic recession, *Nature*, *2*, 1–7, doi:10.1038/srep00265.

Chang, C.-Y., E. Faust, X. Hou, P. Lee, H. C. Kim, B. C. Hedquist, and K.-J. Liao (2016), Investigating ambient ozone formation regimes in neighboring cities of shale plays in the Northeast United States using photochemical modeling and satellite retrievals, *Atmospheric Environment*, 1–44, doi:10.1016/j.atmosenv.2016.06.058.

Cheng, H. R., H. Guo, S. M. Saunders, S. H. M. Lam, F. Jiang, X. M. Wang, I. J. Simpson, D. R. Blake, P. K. K. Louie, and T. J. Wang (2010), Assessing photochemical ozone formation in the Pearl River Delta with a photochemical trajectory model, *Atmospheric Environment*, 44(34), 4199–4208, doi:10.1016/j.atmosenv.2010.07.019.

Choi, Y., H. Kim, D. Tong, and P. Lee (2012), Summertime weekly cycles of observed and modeled NO_x and O_3 concentrations as a function of satellite-derived ozone production sensitivity and land use types over the Continental United States, *Atmos. Chem. Phys.*, *12*(14), 6291–6307, doi:10.5194/acp-12-6291-2012.

Cohan, D. S., A. Hakami, Y. Hu, and A. G. Russell (2005), Nonlinear Response of Ozone to Emissions: Source Apportionment and Sensitivity Analysis, *Environ. Sci. Technol.*, *39*(17), 6739–6748, doi:10.1021/es048664m.

Smedt, I.D., Müller, J.F., Stavrakou, T., Eskes, H. and Roozendael, M.V., (2008). Twelve years of global observations of formaldehyde in the troposphere using GOME and SCIAMACHY sensors. *Atmospheric Chemistry and Physics*, *8*(16), pp.4947-4963, doi:10.5194/acp-8-4947-2008.

De Smedt, I., M. Van Roozendael, T. Stavrakou, J. F. Müller, C. Lerot, N. Theys, P. Valks, N. Hao, and R. van der A (2012), Improved retrieval of global tropospheric formaldehyde columns from GOME-2/MetOp-A addressing noise reduction and instrumental degradation issues, *Atmos. Meas. Tech.*, *5*(11), 2933–2949, doi:10.5194/amt-5-2933-2012.

De Smedt, I. et al. (2015), Diurnal, seasonal and long-term variations of global formaldehyde columns inferred from combined OMI and GOME-2 observations, *Atmos. Chem. Phys.*, *15*(21), 12519–12545, doi:10.5194/acp-15-12519-2015.

Dobber, M., Q. Kleipool, R. Dirksen, P. Levelt, G. Jaross, S. Taylor, T. Kelly, L. Flynn, G. Leppelmeier, and N. Rozemeijer (2008), Validation of Ozone Monitoring Instrument level 1b data products, *J. Geophys. Res.*, *113*(D15), D15S06–12, doi:10.1029/2007JD008665.

Duncan, B. N. et al. (2010), Application of OMI observations to a space-based indicator of NO x and VOC controls on surface O_3 formation, *Atmospheric Environment*, *44*(18), 2213–2223, doi:10.1016/j.atmosenv.2010.03.010.

Duncan, B. N., L. N. Lamsal, A. M. Thompson, Y. Yoshida, Z. Lu, D. G. Streets, M. M. Hurwitz, and K. E. Pickering (2016), A space-based, high-resolution view of notable changes in urban NO_x pollution around the world (2005-2014), *J. Geophys. Res. Atmos.*, *121*(2), 976–996, doi:10.1002/2015JD024121.

Dunker, A. M., G. Yarwood, J. P. Ortmann, and G. M. Wilson (2002), Comparison of Source Apportionment and Source Sensitivity of Ozone in a Three-Dimensional Air Quality Model, *Environ. Sci. Technol.*, *36*(13), 2953–2964, doi:10.1021/es011418f.

Eskes, H. J., and K. F. Boersma (2003), Averaging kernels for DOAS total-column satellite retrievals, *Atmos. Chem. Phys.*, *3*(5), 1285–1291, doi:10.5194/acp-3-1285-2003.

Frost, G. J. et al. (2006), Effects of changing power plant NO_x emissions on ozone in the eastern United States: Proof of concept, *J. Geophys. Res.*, *111*(D12), D12306–19, doi:10.1029/2005JD006354.

Fu, J. S., X. Dong, Y. Gao, D. C. Wong, and Y. F. Lam (2012), Sensitivity and linearity analysis of O_3 in East Asia: The effects of domestic emission and intercontinental transport, *Journal of the Air & Waste Management Association*, *62*(9), 1102–1114, doi:10.1080/10962247.2012.699014.

González Abad, G., X. Liu, K. Chance, H. Wang, T. P. Kurosu, and R. Suleiman (2015), Updated Smithsonian Astrophysical Observatory Ozone Monitoring Instrument (SAO OMI) formaldehyde retrieval, *Atmos. Meas. Tech.*, *8*(1), 19–32, doi:10.5194/amt-8-19-2015.

Gu, D., Y. Wang, C. Smeltzer, and Z. Liu (2013), Reduction in NOx Emission Trends over China: Regional and Seasonal Variations, *Environ. Sci. Technol.*, *47*(22), 12912–12919, doi:10.1021/es401727e.

Guenther, A., T. Karl, P. Harley, C. Wiedinmyer, P. I. Palmer, and C. Geron (2006), Estimates of global terrestrial isoprene emissions using MEGAN (Model of Emissions of Gases and Aerosols from Nature), *Atmos. Chem. Phys.*, *6*(1), 3181–3210, doi:10.5194/acp-6-3181-2006.

Guenther, A. B., X. Jiang, C. L. Heald, T. Sakulyanontvittaya, T. Duhl, L. K. Emmons, and X. Wang (2012), The Model of Emissions of Gases and Aerosols from Nature version 2.1 (MEGAN2.1): an extended and updated framework for modeling biogenic emissions, *Geosci. Model Dev.*, *5*(6), 1471–1492, doi:10.5194/gmd-5-1471-2012.

Guerreiro, C. B. B., V. Foltescu, and F. de Leeuw (2014), Air quality status and trends in Europe, *Atmospheric Environment*, *98*(c), 376–384, doi:10.1016/j.atmosenv.2014.09.017.

Hakami, A., J. H. Seinfeld, T. Chai, Y. Tang, G. R. Carmichael, and A. Sandu (2006), Adjoint Sensitivity Analysis of Ozone Nonattainment over the Continental United States, *Environ. Sci. Technol.*, *40*(12), 3855–3864, doi:10.1021/es052135g.

Halla, J. D., T. Wagner, S. Beirle, J. R. Brook, K. L. Hayden, J. M. O'Brien, A. Ng, D. Majonis, M. O. Wenig, and R. McLaren (2011), Determination of tropospheric vertical columns of NO_2 and aerosol optical properties in a rural setting using MAX-DOAS, *Atmos. Chem. Phys.*, *11*(23), 12475–12498, doi:10.5194/acp-11-12475-2011.

Hammer, M. U. (2002), Findings on H_2O_2/HNO_3 as an indicator of O_3 sensitivity in Baden-Württemberg, Berlin-Brandenburg, and the Po valley based on numerical simulations, *J. Geophys. Res.*, *107*(D22), 8190–18, doi:10.1029/2000JD000211.

Hudman, R. C., N. E. Moore, A. K. Mebust, R. V. Martin, A. R. Russell, L. C. Valin, and R. C. Cohen (2012), Steps towards a mechanistic model of global soil nitric oxide emissions: implementation and space based-constraints, *Atmos. Chem. Phys.*, *12*(16), 7779–7795, doi:10.5194/acp-12-7779-2012.

Iqbal, M. A., K.-H. Kim, Z.-H. Shon, J.-R. Sohn, E.-C. Jeon, Y.-S. Kim, and J.-M. Oh (n.d.), Comparison of ozone pollution levels at various sites in Seoul, a megacity in Northeast Asia, *Atmospheric Research*, *138 IS* -, 330–345, doi: 10.1016/j.atmosres.2013.12.003.

Jacob, D. J., L. W. Horowitz, J. W. Munger, B. G. Heikes, R. R. Dickerson, R. S. Artz, and W. C. Keene (1995), Seasonal transition from NO_x- to hydrocarbon-limited conditions for ozone production over the eastern United States in September, *J. Geophys. Res.*, *100*(D5), 9315–11, doi:10.1029/94JD03125.

Jin, X., and T. Holloway (2015), Spatial and temporal variability of ozone sensitivity over China observed from the Ozone Monitoring Instrument, *J. Geophys. Res. Atmos.*, *120*(14), 7229–7246, doi:10.1002/2015JD023250.

Jing, P., Z. Lu, J. Xing, D. G. Streets, Q. Tan, T. O'Brien, and J. Kamberos (2014), Response of the summertime ground-level ozone trend in the Chicago area to emission controls and temperature changes, 2005-2013, *Atmospheric Environment*, *99*(C), 630–640, doi:10.1016/j.atmosenv.2014.10.035.

Kampa, M., and E. Castanas (2008), Human health effects of air pollution, *Environmental Pollution*, *151*(2), 362–367, doi:10.1016/j.envpol.2007.06.012.

Kleinman, L. I. (1991), Seasonal dependence of boundary layer peroxide concentration: The low and high NOx regimes, *Journal of Geophysical Research: Atmospheres (1984–2012)*, *96*(D11), 20721–20733, doi:10.1029/91JD02040.

Kleinman, L. I. (1994), Low and High NO_x Tropospheric Photochemistry, *J. Geophys. Res. Atmos.*, *99*(D8), 16831–16838, doi:10.1029/94JD01028.

Kommalapati, R. R., Z. Liang, and Z. Huque (2015), Photochemical model simulations of air quality for Houston–Galveston–Brazoria area and analysis of ozone–NOx–hydrocarbon sensitivity, *Int. J. Environ. Sci. Technol.*, *13*(1), 209–220, doi:10.1007/s13762-015-0862-6.

Kuhns, H., E. M. Knipping, and J. M. Vukovich (2005), Development of a United States–Mexico Emissions Inventory for the Big Bend Regional Aerosol and Visibility Observational (BRAVO) Study, *Journal of the Air & Waste Management Association*, *55*(5), 677–692, doi:10.1080/10473289.2005.10464648.

LaFranchi, B. W., A. H. Goldstein, and R. C. Cohen (2011), Observations of the temperature dependent response of ozone to NO_x reductions in the Sacramento, CA urban plume, *Atmos. Chem. Phys.*, 11(14), 6945–6960, doi:10.5194/acp-11-6945-2011.

Lahoz, W. A. et al. (2012), Monitoring Air Quality from Space: The Case for the Geostationary Platform, *Bull. Amer. Meteor. Soc.*, *93*(2), 221–233, doi:10.1175/BAMS-D-11-00045.1.

837 Lamsal, L. N., R. V. Martin, A. van Donkelaar, M. Steinbacher, E. A. Celarier, E. Bucsela, E. J.
838 Dunlea, and J. P. Pinto (2008), Ground-level nitrogen dioxide concentrations inferred from
839 the satellite-borne Ozone Monitoring Instrument, *J. Geophys. Res.*, *113*(D16), D05204–15,
840 doi:10.1029/2007JD009235.
841 Lamsal, L. N. et al. (2014), Evaluation of OMI operational standard NO_2 column retrievals using
842 in situ and surface-based NO_2 observations, *Atmos. Chem. Phys.*, *14*(21), 11587–11609,
843 doi:10.5194/acp-14-11587-2014.
844 Lamsal, L. N., B. N. Duncan, Y. Yoshida, N. A. Krotkov, K. E. Pickering, D. G. Streets, and Z.
845 Lu (2015), U.S. NO_2 trends (2005-2013): EPA Air Quality System (AQS) data versus
846 improved observations from the Ozone Monitoring Instrument (OMI), *Atmospheric*
847 *Environment*, *110*(C), 130–143, doi:10.1016/j.atmosenv.2015.03.055.
848 Lefohn, A. S., C. S. Malley, H. Simon, B. Wells, X. Xu, L. Zhang, and T. Wang (2017),
849 Responses of human health and vegetation exposure metrics to changes in ozone
850 concentration distributions in the European Union, United States, and China, *Atmospheric*
851 *Environment*, *152*, 123–145, doi:10.1016/j.atmosenv.2016.12.025.
852 Lelieveld, J., C. Barlas, D. Giannadaki, and A. Pozzer (2013), Model calculated global, regional
853 and megacity premature mortality due to air pollution, *Atmos. Chem. Phys.*, *13*(14), 7023–
854 7037, doi:10.5194/acp-13-7023-2013.
855 Levelt, P. F., G. H. J. van den Oord, M. R. Dobber, A. Malkki, Huib Visser, Johan de Vries, P.
856 Stammes, J. O. V. Lundell, and H. Saari (2006), The Ozone monitoring instrument,
857 *Geoscience and Remote Sensing, IEEE Transactions on*, *44*(5), 1093–1101,
858 doi:10.1109/TGRS.2006.872333.
859 Li, Y., A. K. H. Lau, J. C. H. Fung, J. Zheng, and S. Liu (2013), Importance of NO_x control for
860 peak ozone reduction in the Pearl River Delta region, *J. Geophys. Res. Atmos.*, 118(16),
861 9428–9443, doi:10.1002/jgrd.50659.
862 Li, Y., A. K. H. Lau, J. C. H. Fung, J. Y. Zheng, L. J. Zhong, and P. K. K. Louie (2012), Ozone
863 source apportionment (OSAT) to differentiate local regional and super-regional source
864 contributions in the Pearl River Delta region, China, *J. Geophys. Res.*, *117*, D15305,
865 doi:10.1029/2011JD017340.
866 Lin, J.-T., and M. B. McElroy (2010), Impacts of boundary layer mixing on pollutant vertical
867 profiles in the lower troposphere: Implications to satellite remote sensing, *Atmospheric*
868 *Environment*, *44*(14), 1726–1739, doi:10.1016/j.atmosenv.2010.02.009.
869 Lin, J.-T., R. V. Martin, K. F. Boersma, M. Sneep, P. Stammes, R. Spurr, P. Wang, M. Van
870 Roozendael, K. Clémer, and H. Irie (2014), Retrieving tropospheric nitrogen dioxide from
871 the Ozone Monitoring Instrument: effects of aerosols, surface reflectance anisotropy, and
872 vertical profile of nitrogen dioxide, *Atmos. Chem. Phys.*, *14*(3), 1441–1461,
873 doi:10.5194/acp-14-1441-2014.
874 Lin, J.-T., M. Y. Liu, J. Y. Xin, K. F. Boersma, R. Spurr, R. Martin, and Q. Zhang (2015),
875 Influence of aerosols and surface reflectance on satellite NO_2 retrieval: seasonal and spatial
876 characteristics and implications for NO_x emission constraints, *Atmos. Chem. Phys.*, *15*(19),
877 11217–11241, doi:10.5194/acp-15-11217-2015.
878 Liu, F., Q. Zhang, R. J. van der A, B. Zheng, D. Tong, L. Yan, Y. Zheng, and K. He (2016),
879 Recent reduction in NO_x emissions over China: synthesis of satellite observations and
880 emission inventories, *Environ. Res. Lett.*, *11*(11), 114002–10, doi:10.1088/1748-
881 9326/11/11/114002.

Liu, H., X. M. Wang, J. M. Pang, and K. B. He (2013), Feasibility and difficulties of China's new air quality standard compliance: PRD case of $PM_{2.5}$ and O_3 from 2010 to 2025, *Atmos. Chem. Phys.*, *13*(23), 12013–12027, doi:10.5194/acp-13-12013-2013.

Liu, X.-H., Y. Zhang, J. Xing, Q. Zhang, K. Wang, D. G. Streets, C. Jang, W.-X. Wang, and J.-M. Hao (2010), Understanding of regional air pollution over China using CMAQ, part II. Process analysis and sensitivity of ozone and particulate matter to precursor emissions, *Atmospheric Environment*, *44*(30), 3719–3727, doi:10.1016/j.atmosenv.2010.03.036.

Liu, Z. *et al*. (2012), Summertime photochemistry during CAREBeijing-2007: ROx budgets and O_3 formation, *Atmos. Chem. Phys.*, 12(16), 7737–7752, doi:10.5194/acp-12-7737-2012.

Lorente, A. et al. (2017), Structural uncertainty in air mass factor calculation for NO_2 and HCHO satellite retrievals, *Atmos. Meas. Tech.*, *10*(3), 759–782, doi:10.5194/amt-10-759-2017.

Lu, K. *et al*. (2010), Oxidant (O_3+NO_2) production processes and formation regimes in Beijing (vol 115, D07303, 2010), *J. Geophys. Res. Atmos.*, 115(D10), doi:10.1029/2010JD014394.

Marais, E. A. et al. (2012), Isoprene emissions in Africa inferred from OMI observations of formaldehyde columns, *Atmos. Chem. Phys.*, *12*(14), 6219–6235, doi:10.5194/acp-12-6219-2012.

Marchenko, S., Krotkov, N. A., Lamsal, L. N., Celarier, E. A., Swartz, W. H., & Bucsela, E. J. (2015), Revising the slant column density retrieval of nitrogen dioxide observed by the Ozone Monitoring Instrument, *J. Geophys. Res. Atmos.*, 120, 5670–5692, doi:10.1002/2014JD022913.

Martin, R V., Arlene M. Fiore, and Aaron Van Donkelaar. (2004a), Space-based diagnosis of surface ozone sensitivity to anthropogenic emissions, *Geophys. Res. Lett.*, *31*(6), L06120, doi:10.1029/2004GL019416.

Martin, R. V., D. D. Parrish, T. B. Ryerson, D. K. Nicks, K. Chance, T. P. Kurosu, Daniel James Jacob, E. D. Sturges, A. Fried, and B. P. Wert. (2004b), Evaluation of GOME satellite measurements of tropospheric NO_2 and HCHO using regional data from aircraft campaigns in the southeastern United States, *J. Geophys. Res.*, *109*(D24), D24307–11, doi:10.1029/2004JD004869.

Mazzuca, G. M., X. Ren, C. P. Loughner, M. Estes, J. H. Crawford, K. E. Pickering, A. J. Weinheimer, and R. R. Dickerson (2016), Ozone production and its sensitivity to NOx and VOCs: results from the DISCOVER-AQ field experiment, Houston 2013, *Atmos. Chem. Phys.*, *16*(22), 14463–14474, doi:10.5194/acp-16-14463-2016.

Millet, D. B., D. J. Jacob, K. F. Boersma, T.-M. Fu, T. P. Kurosu, K. Chance, C. L. Heald, and A. Guenther (2008), Spatial distribution of isoprene emissions from North America derived from formaldehyde column measurements by the OMI satellite sensor, *Journal of Geophysical Research: Atmospheres (1984–2012)*, *113*(D2), D02307, doi:10.1029/2007JD008950.

Murray, L. T. (2016), Lightning NOx and Impacts on Air Quality, *Curr Pollution Rep*, *2*(2), 115–133, doi:10.1007/s40726-016-0031-7.

Olivier, J. G. J., J. A. Van Aardenne, F. J. Dentener, V. Pagliari, L. N. Ganzeveld, and J. A. H. W. Peters (2007), Recent trends in global greenhouse gas emissions:regional trends 1970–2000 and spatial distributionof key sources in 2000, *Environmental Sciences*, *2*(2-3), 81–99, doi:10.1080/15693430500400345.

Pan, X., Y. Kanaya, H. Tanimoto, S. Inomata, Z. Wang, S. Kudo, and I. Uno (2015), Examining the major contributors of ozone pollution in a rural area of the Yangtze River Delta region during harvest season, *Atmos. Chem. Phys.*, 15(11), 6101–6111, doi:10.5194/acp-15-6101-2015.

Pusede, S. E., A. L. Steiner, and R. C. Cohen (2015), Temperature and Recent Trends in the Chemistry of Continental Surface Ozone, *Chem. Rev.*, *115*(10), 3898–3918, doi:10.1021/cr5006815.

Pusede, S. E., and R. C. Cohen (2012), On the observed response of ozone to NO_x and VOC reactivity reductions in San Joaquin Valley California 1995–present, *Atmos. Chem. Phys.*, 12(18), 8323–8339, doi:10.5194/acp-12-8323-2012.

Rienecker, M. M. et al. (2011), MERRA: NASA's Modern-Era Retrospective Analysis for Research and Applications, *J. Climate*, *24*(14), 3624–3648, doi:10.1175/JCLI-D-11-00015.1.

Schmidt, H. (2003), Adjoint sensitivity of episodic ozone in the Paris area to emissions on the continental scale, *J. Geophys. Res.*, *108*(D17), 8561–16, doi:10.1029/2001JD001583.

Schneider, P., W. A. Lahoz, and R. van der A (2015), Recent satellite-based trends of tropospheric nitrogen dioxide over large urban agglomerations worldwide, *Atmos. Chem. Phys.*, *15*(3), 1205–1220, doi:10.5194/acp-15-1205-2015.

Schultz, M. G., *et al.* (2007), REanalysis of the TROpospheric chemical composition over the past 40 years (RETRO) — A long-term global modeling study of tropospheric chemistry Rep., Max Planck Institute for Meteorology, Jülich/Hamburg, Germany.

Sillman, S. (1995), The use of NO_y, H_2O_2, and HNO_3 as indicators for O_3-NO_x -hydrocarbon sensitivity in urban locations, *Journal of Geophysical Research: Atmospheres (1984–2012)*, *100*(D7), 14175–14188, doi:10.1029/94JD02953.

Sillman, S. (2002), Some theoretical results concerning O_3-NO_x -VOC chemistry and NO_x-VOC indicators, *J. Geophys. Res.*, *107*(D22), 4659–15, doi:10.1029/2001JD001123.

Simon, H., A. Reff, B. Wells, J. Xing, and N. Frank (2015), Ozone Trends Across the United States over a Period of Decreasing NO_x and VOC Emissions, *Environ. Sci. Technol.*, *49*(1), 186–195, doi:10.1021/es504514z.

Song, J., W. Lei, N. Bei, M. Zavala, B. de Foy, R. Volkamer, B. Cardenas, J. Zheng, R. Zhang, and L. T. Molina (2010), Ozone response to emission changes: a modeling study during the MCMA-2006/MILAGRO Campaign, *Atmos. Chem. Phys.*, *10*(8), 3827–3846, doi:10.5194/acp-10-3827-2010.

Souri, A. H., Y. Choi, W. Jeon, J.-H. Woo, Q. Zhang, and J.-I. Kurokawa (2017), Remote sensing evidence of decadal changes in major tropospheric ozone precursors over East Asia, *J. Geophys. Res. Atmos.*, *122*(4), 2474–2492, doi:10.1002/2016JD025663.

Spurr, R. (2008), LIDORT and VLIDORT: Linearized pseudo-spherical scalar and vector discrete ordinate radiative transfer models for use in remote sensing retrieval problems, in *Light Scattering Reviews 3*, pp. 229–275, Springer Berlin Heidelberg, Berlin, Heidelberg.

Stein, A. F., E. Mantilla, and M. M. Millán (2005), Using measured and modeled indicators to assess O_3-NO_x-VOC sensitivity in a western Mediterranean coastal environment, *Atmospheric Environment*, *39*(37), 7167–7180, doi:10.1016/j.atmosenv.2005.08.026.

Stettler, M. E. J., S. Eastham, and S. R. H. Barrett (2011), Air quality and public health impacts of UK airports. Part I: Emissions, *Atmospheric Environment*, *45*(31), 5415–5424, doi:10.1016/j.atmosenv.2011.07.012.

969 Streets, D. G., Q. Zhang, L. Wang, K. He, J. Hao, Y. Wu, Y. Tang, and G. R. Carmichael (2006),
970 Revisiting China's CO emissions after the Transport and Chemical Evolution over the
971 Pacific (TRACE-P) mission: Synthesis of inventories, atmospheric modeling, and
972 observations, *J. Geophys. Res.*, *111*(D14), D14306–16, doi:10.1029/2006JD007118.
973 Tong, D. Q., L. Lamsal, L. Pan, C. Ding, H. Kim, P. Lee, T. Chai, K. E. Pickering, and I. Stajner
974 (2015), Long-term NO_x trends over large cities in the United States during the great
975 recession: Comparison of satellite retrievals, ground observations, and emission inventories,
976 *Atmospheric Environment*, *107*(c), 70–84, doi:10.1016/j.atmosenv.2015.01.035.
977 Tonnesen, G. S., and R. L. Dennis (2000), Analysis of radical propagation efficiency to assess O_3
978 sensitivity to hydrocarbons and NO_x: 2. Long-lived species as indicators of O_3 concentration
979 sensitivity, *Journal of Geophysical Research: Atmospheres (1984–2012)*, *105*(D7), 9227–
980 9241, doi:10.1029/1999JD900372.
981 Travis, K. R. et al. (2016), Why do models overestimate surface ozone in the Southeast United
982 States? *Atmos. Chem. Phys.*, *16*(21), 13561–13577, doi:10.5194/acp-16-13561-2016.
983 Valin, L. C., A. M. Fiore, K. Chance, and G. Gonzalez Abad (2016), The role of OH production
984 in interpreting the variability of CH2O columns in the southeast US, *Journal of Geophysical*
985 *Research: Atmospheres*, doi:10.1002/(ISSN)2169-8996.
986 Van Dingenen, R., F. J. Dentener, F. Raes, M. C. Krol, L. Emberson, and J. Cofala (2009),
987 Atmospheric Environment, *Atmospheric Environment*, *43*(3), 604–618,
988 doi:10.1016/j.atmosenv.2008.10.033.
989 van Donkelaar, A. et al. (2008), Analysis of aircraft and satellite measurements from the
990 Intercontinental Chemical Transport Experiment (INTEX-B) to quantify long-range
991 transport of East Asian sulfur to Canada, *Atmos. Chem. Phys.*, *8*(11), 2999–3014,
992 doi:10.5194/acp-8-2999-2008.
993 van der Werf, G. R., J. T. Randerson, L. Giglio, G. J. Collatz, M. Mu, P. S. Kasibhatla, D. C.
994 Morton, R. S. DeFries, Y. Jin, and T. T. van Leeuwen (2010), Global fire emissions and the
995 contribution of deforestation, savanna, forest, agricultural, and peat fires (1997–2009),
996 *Atmos. Chem. Phys.*, *10*(23), 11707–11735, doi:10.5194/acp-10-11707-2010.
997 Vinken, G. C. M., K. F. Boersma, D. J. Jacob, and E. W. Meijer (2011), Accounting for non-
998 linear chemistry of ship plumes in the GEOS-Chem global chemistry transport model,
999 *Atmos. Chem. Phys.*, *11*(22), 11707–11722, doi:10.5194/acp-11-11707-2011.
1000 Vogel, B., N. Riemer, H. Vogel, and F. Fiedler (2007), Findings on NO_y as an indicator for ozone
1001 sensitivity based on different numerical simulations, *J. Geophys. Res.*, 104(D3), 3605–3620,
1002 doi:10.1029/1998JD100075.
1003 Wang, Q., Z. Han, T. Wang, and R. Zhang (2008), Impacts of biogenic emissions of VOC and
1004 NOx on tropospheric ozone during summertime in eastern China, *Science of The Total*
1005 *Environment*, 395(1), 41–49, doi:10.1016/j.scitotenv.2008.01.059.
1006 Wang, T., A. Ding, J. Gao, and W. S. Wu (2006), Strong ozone production in urban plumes from
1007 Beijing, China, *Geophys. Res. Lett.*, 33(21), L21806, doi:10.1029/2006GL027689.
1008 Wang, Y., J. Hao, M. B. McElroy, J. W. Munger, H. Ma, D. Chen, and C. P. Nielsen (2009),
1009 Ozone air quality during the 2008 Beijing Olympics: effectiveness of emission restrictions,
1010 *Atmos. Chem. Phys.*, *9*(14), 5237–5251, doi:10.5194/acp-9-5237-2009.

Wolfe, G. M. et al. (2016), Formaldehyde production from isoprene oxidation across NO_x regimes, *Atmos. Chem. Phys.*, *16*(4), 2597–2610, doi:10.5194/acp-16-2597-2016.

Wu, S., B. N. Duncan, D. J. Jacob, A. M. Fiore, and O. Wild (2009), Chemical nonlinearities in relating intercontinental ozone pollution to anthropogenic emissions, *Geophys. Res. Lett.*, *36*(5), L05806, doi:10.1029/2008GL036607.

Xing, J., S. X. Wang, C. Jang, Y. Zhu, and J. M. Hao (2011), Nonlinear response of ozone to precursor emission changes in China: a modeling study using response surface methodology, *Atmos. Chem. Phys.*, 11(10), 5027–5044, doi:10.5194/acp-11-5027-2011.

Xue, L.K., T. Wang, J. Gao, A. J. Ding, X. H. Zhou, D. R. Blake, X. F. Wang, S. M. Saunders, S. J. Fan, H. C. Zuo, Q. Z. Zhang (2014), Ground-level ozone in four Chinese cities: precursors, regional transport and heterogeneous processes, *Atmos. Chem. Phys.*, 14(23), 13175–13188, doi:10.5194/acp-14-13175-2014.

Ye, L., X. Wang, S. Fan, W. Chen, M. Chang, S. Zhou, Z. Wu, and Q. Fan (2016), Photochemical indicators of ozone sensitivity: application in the Pearl River Delta, China, *Front. Environ. Sci. Eng.*, 10(6), 11803–14, doi:10.1007/s11783-016-0887-1.

Yue, X., and N. Unger (2014), Ozone vegetation damage effects on gross primary productivity in the United States, *Atmos. Chem. Phys.*, *14*(17), 9137–9153, doi:10.5194/acp-14-9137-2014.

Zhang, L., D. J. Jacob, M. Kopacz, D. K. Henze, K. Singh, and D. A. Jaffe (2009), Intercontinental source attribution of ozone pollution at western U.S. sites using an adjoint method, *Geophys. Res. Lett.*, *36*(11), L11810–5, doi:10.1029/2009GL037950.

Zhang, Q., D. G. Streets, G. R. Carmichael, K. B. He, H. Huo, A. Kannari, Z. Klimont, I. S. Park, S. Reddy, J. S. Fu, D. Chen, L. Duan, Y. Lei, L. T. Wang, and Z. L. Yao (2009), Asian emissions in 2006 for the NASA INTEX-B mission, *Atmos. Chem. Phys.*, *9*(14), 5131–5153, doi:10.5194/acp-9-5131-2009.

Zhang, Y., Y. Wang, G. Chen, C. Smeltzer, J. Crawford, J. Olson, J. Szykman, A. J. Weinheimer, D. J. Knapp, D. D. Montzka, et al. (2016), Large vertical gradient of reactive nitrogen oxides in the boundary layer: Modeling analysis of DISCOVER-AQ 2011 observations, *J. Geophys. Res. Atmos.*, 121, 1922–1934, doi:10.1002/2015JD024203.

Zhu, L., D. J. Jacob, P. S. Kim, J. A. Fisher, K. Yu, K. R. Travis, L. J. Mickley, R. M. Yantosca, M. P. Sulprizio, I. D. Smedt, G. Abad, K. Chance, C. Li, R. Ferrare, A. Fried, J. W. Hair, T. F. Hanisco, D. Richter, A. J. Scarino, J. Walega, P. Weibring, G. M. Wolfe (2016), Observing atmospheric formaldehyde (HCHO) from space: validation and intercomparison of six retrievals from four satellites (OMI, GOME2A, GOME2B, OMPS) with SEAC^{4}RS aircraft observations over the Southeast US, *Atmos. Chem. Phys.*, 16, 13477-13490, doi:10.5194/acp-16-13477-2016.

Zhu, L., D. J. Jacob, F. N. Keutsch, L. J. Mickley, R. Scheffe, M. Strum, G. Abad, K. Chance, K. Yang, B. Rappenglück, D. B. Millet, M. Baasandorj, L. Jaeglé, V. Shah (2017), Formaldehyde (HCHO) As a Hazardous Air Pollutant: Mapping Surface Air Concentrations from Satellite and Inferring Cancer Risks in the United States, *Environ. Sci. Technol.*, *51*(10), 5650–5657, doi:10.1021/acs.est.7b01356.

Figures List

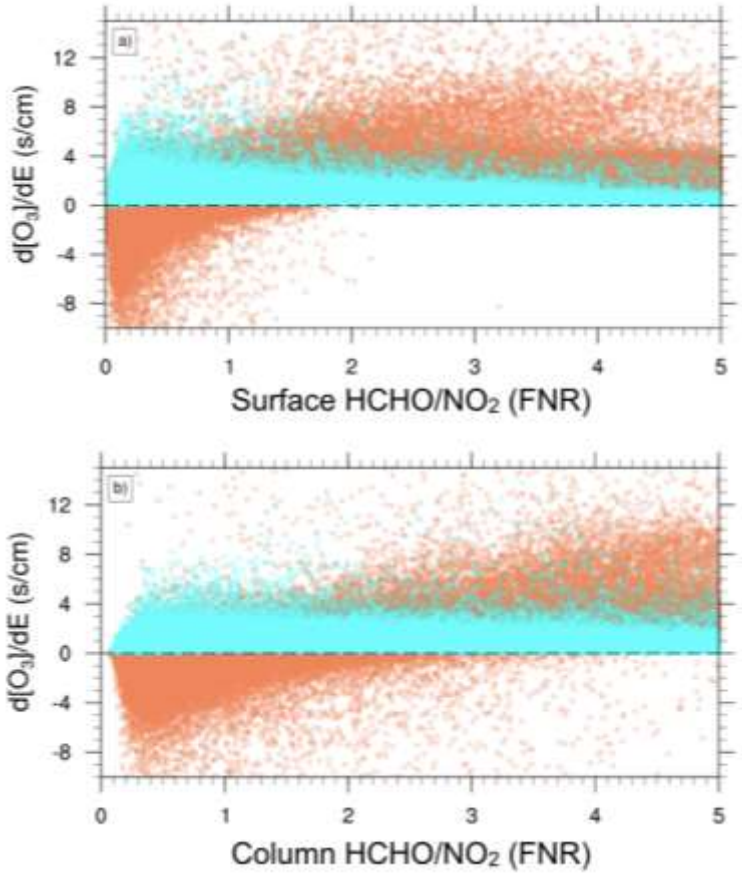

Figure 1 GEOS-Chem model estimates of the normalized ozone sensitivity to 20% decreases in global NO_x and VOC emissions ($d[O_3]/dE_{NOx}$ in orange, $d[O_3]/dE_{VOC}$ in blue) in units of molecules $cm^{-2}s^{-1}$, versus the modeled (a) surface $HCHO/NO_2$ and (b) tropospheric column $HCHO/NO_2$ aggregated over the three selected regions (North America, Europe, Asia). Each point is equal to the normalized sensitivity ratios of daily one-hour averages between 1 and 2 PM from 2006 to 2012 in a single model grid cell. We only include polluted grid cells, defined as cells with average modeled tropospheric NO_2 column densities higher than 2.5×10^{15} molecules/cm^2.

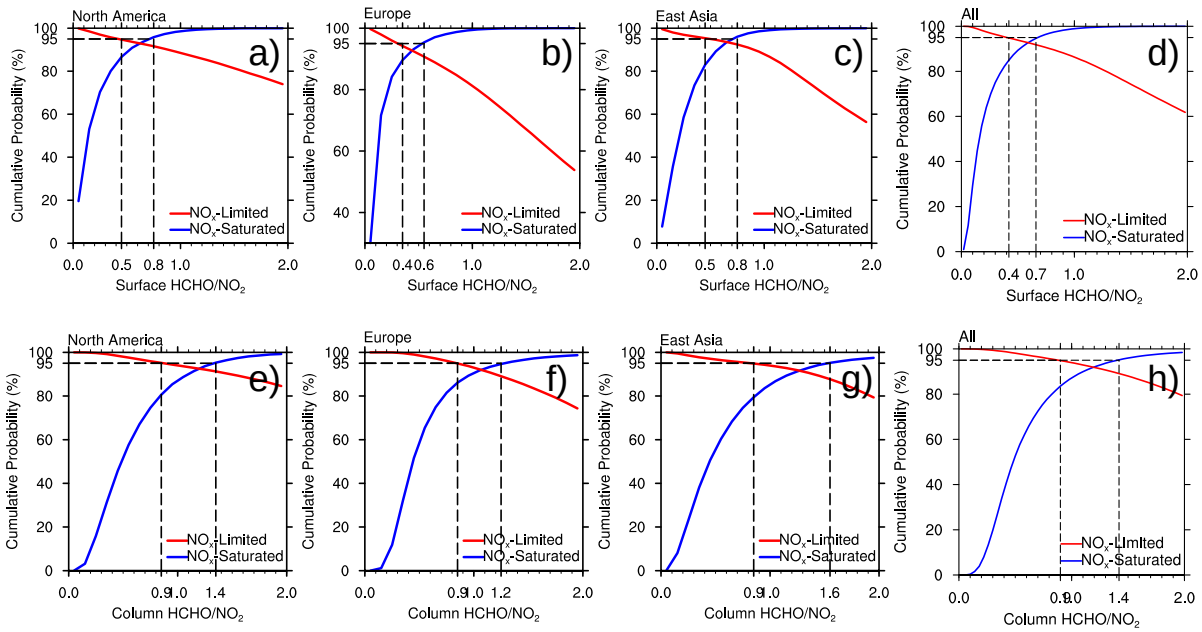

Figure 2 Cumulative probability of NO_x-saturated ($d[O_3]/dE_{NOx} < 0$) and NO_x-limited ($d[O_3]/dE_{NOx} > d[O_3]/dE_{VOC} > 0$) conditions, as a function of modeled (a-d) surface $HCHO/NO_2$ and (e-h) tropospheric column $HCHO/NO_2$ over (a, e) North America, (b, f) Europe, (c, g) East Asia and (d, h) all three regions aggregated, selecting for polluted conditions as in Figure 1. The blue line represents the cumulative probability of NO_x-saturated conditions for all $HCHO/NO_2$ smaller than each given value. The red line represents the cumulative probability of NO_x-limited condition for $HCHO/NO_2$ greater than each given value. The cumulative probability indicates the likelihood of correctly identifying the NO_x-limited or the NO_x-saturated conditions at any given $HCHO/NO_2$ as simulated by the GEOS-Chem model. The probability is calculated from the normalized sensitivity ratios of daily one-hour averages between 1 and 2 PM from 2006 to 2012 (individual points in Figure 1).

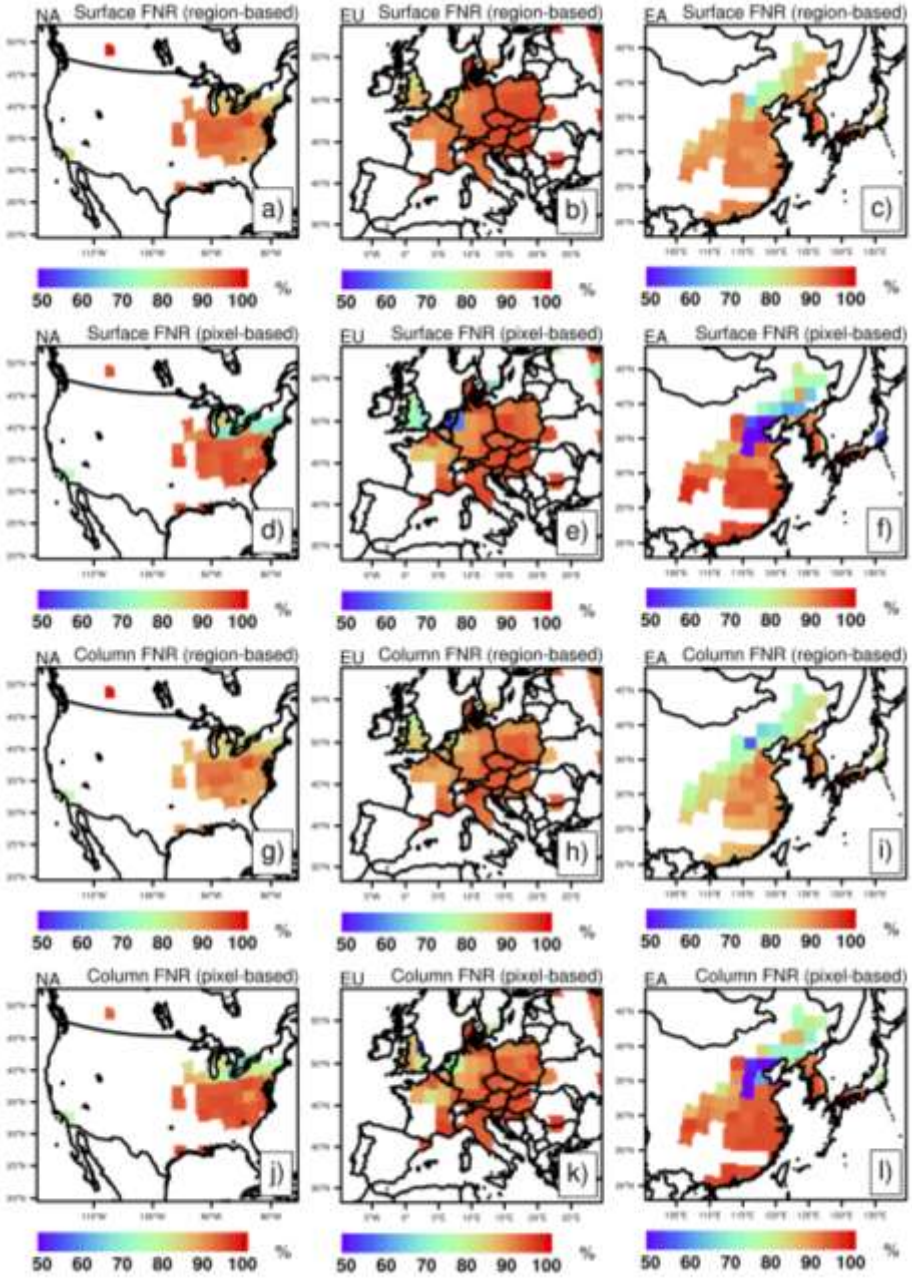

Figure 3 Percentage of correct classifications based on modeled (top two rows) surface or (bottom two rows) column FNR to NO_x-saturated or NO_x-limited conditions using: (first and third rows) regionally-derived values marking the boundary of the transitional regime (second and fourth rows) pixel-based derivation of the transitional regime range over North America (first column), Europe (second column), East Asia (third column). We only include polluted grid cells, defined as cells with average modeled tropospheric NO_2 column densities higher than 2.5×10^{15} molecules/cm^2.

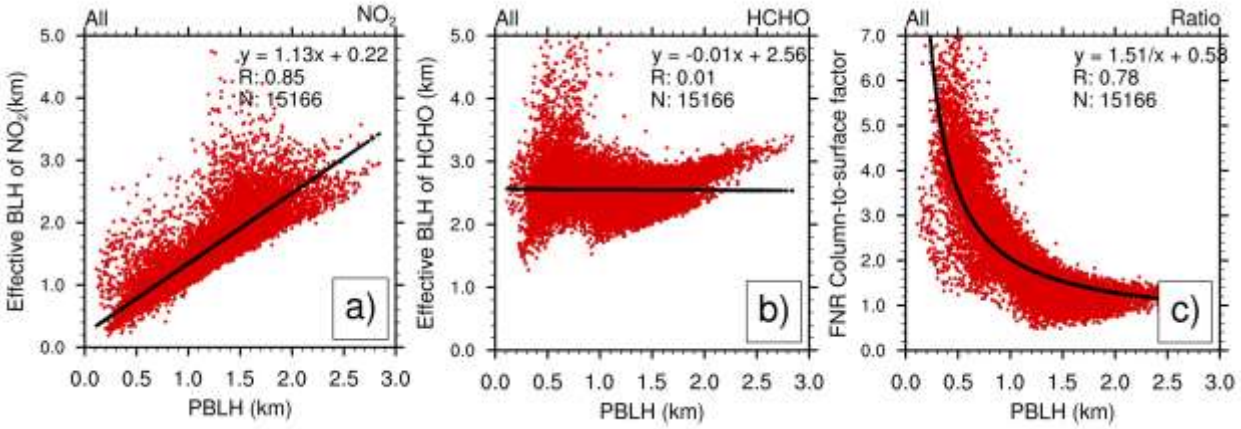

1089

1090 Figure 4 Modeled effective boundary layer height of NO_2 (a) and HCHO (b), column-to-surface
1091 conversion factor of FNR (c), versus planetary boundary layer height (PBLH) over polluted areas
1092 within the three regions (defined as in Figure 1). Each point is the GEOS-Chem daily one-hour
1093 average from 1 to 2 PM. The black lines are the best-fit linear regression (a and b) and reciprocal
1094 regression (c).

1095

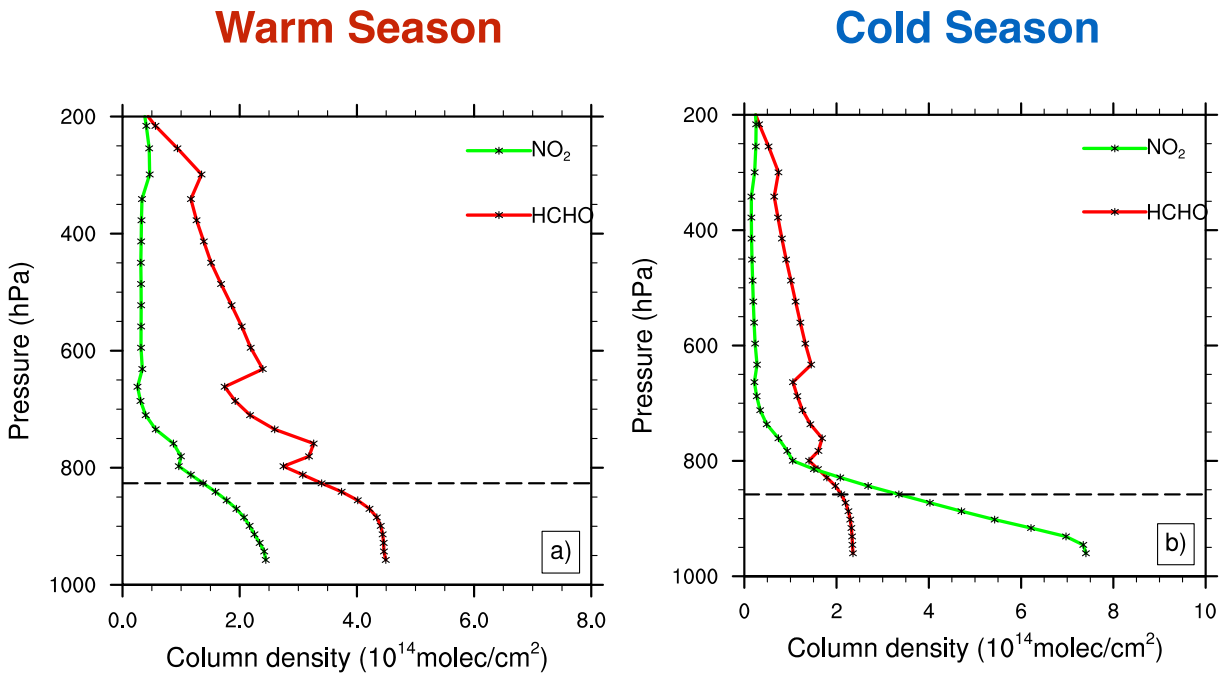

Figure 5 Vertical profiles of HCHO and NO_2 sub-column densities averaged from daily one-hour data between 1 and 2 PM for the warm season (May to September, a) and cold season (October to April, b) from 2005 to 2012 over the polluted areas of three regions aggregated. The dash line shows the average planetary boundary layer height.

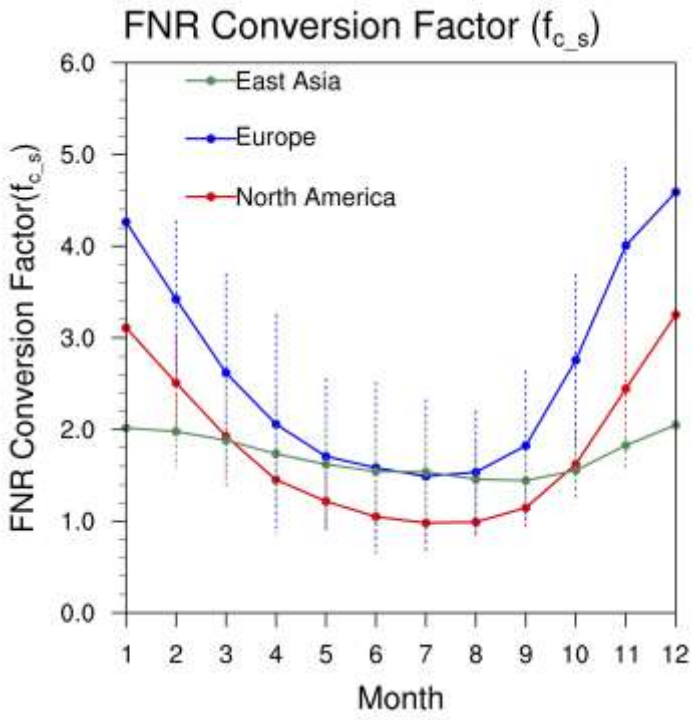

Figure 6 Seasonal cycle of the column-to-surface conversion factors of FNR (f_{c_s}) over North America, Europe and East Asia averaged from daily GEOS-Chem data for polluted areas (modeled tropospheric NO_2 column density higher than 2.5×10^{15} molecules/cm^2) from 2005 to 2012. The dashed error bars are 1σ standard deviation representing spatial variations.

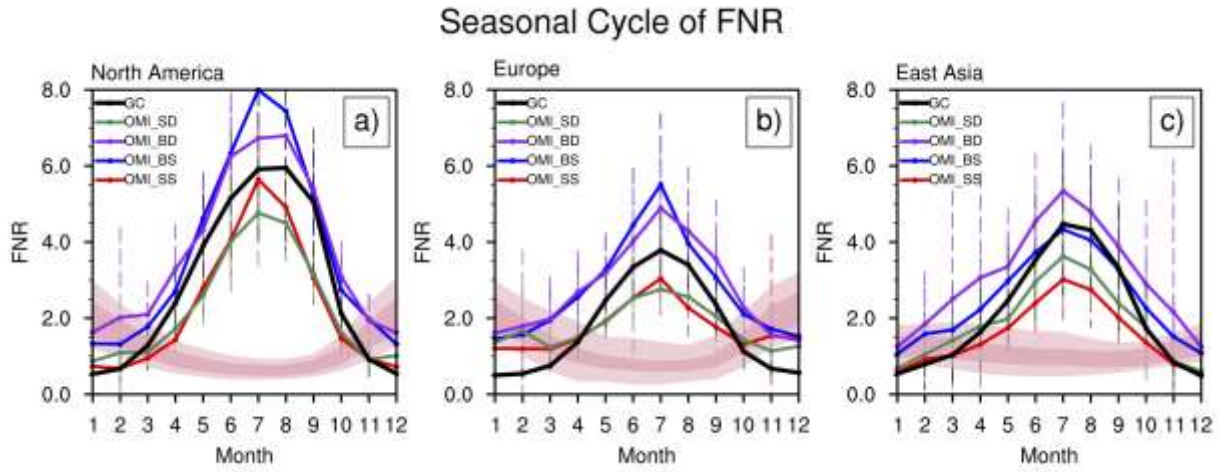

Figure 7 Seasonal cycle of GEOS-Chem modeled (black) and four combinations of OMI observed FNR: 1) SAO HCHO : SP NO_2 (OMI_SS); 2) BIRA HCHO : SP NO_2 (OMI_BS); 3) BIRA HCHO : DP NO_2 (OMI_BD); 4) SAO HCHO : DP NO_2 (OMI_SD), along with the seasonal cycle of column-based regime thresholds in over a) North America, b) Europe, and c) East Asia averaged for polluted areas (modeled tropospheric NO_2 column density higher than 2.5 $\times 10^{15}$ molecules/cm^2) from 2005 to 2012. The dash error bars and the lighter pink band are 1σ standard deviation representing spatial variations.

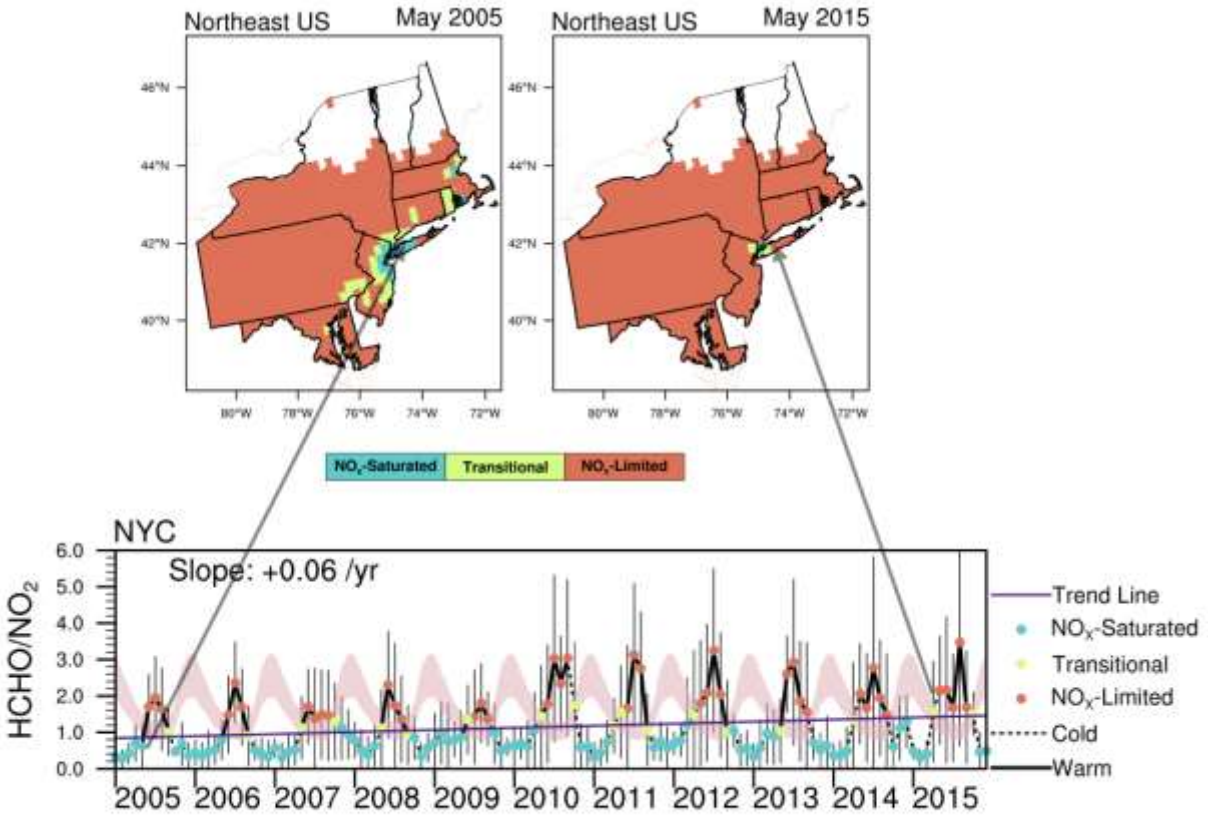

Figure 8 Ozone production regimes over Northeast US in May 2005 and 2015 (top), and time series of OMI-derived FNR along with the regime threshold values (pink shading) in New York City. The regime classification uses the ratio of monthly average OMI Level-3 BIRA HCHO to Level-3 NASA SP NO_2. Solid lines indicate the warm season (May to September) and the dashed lines indicate the cold season (October to April). The transition regime threshold values are adjusted based on the column-to-surface relationships (Section 3.2), and the model-satellite difference (Section 3.3). The observed FNR are monthly average OMI Level-3 BIRA HCHO to Level-3 NASA SP NO_2 for the grid cells fully covering these cities. The uncertainty (error bars) is calculated from monthly standard deviation of NO_2 and HCHO using Equation (3). The blue line shows the linear regression trend. Areas with average observed tropospheric NO_2 column densities $< 2.5 \times 10^{15}$ molecules/cm^2 are masked.

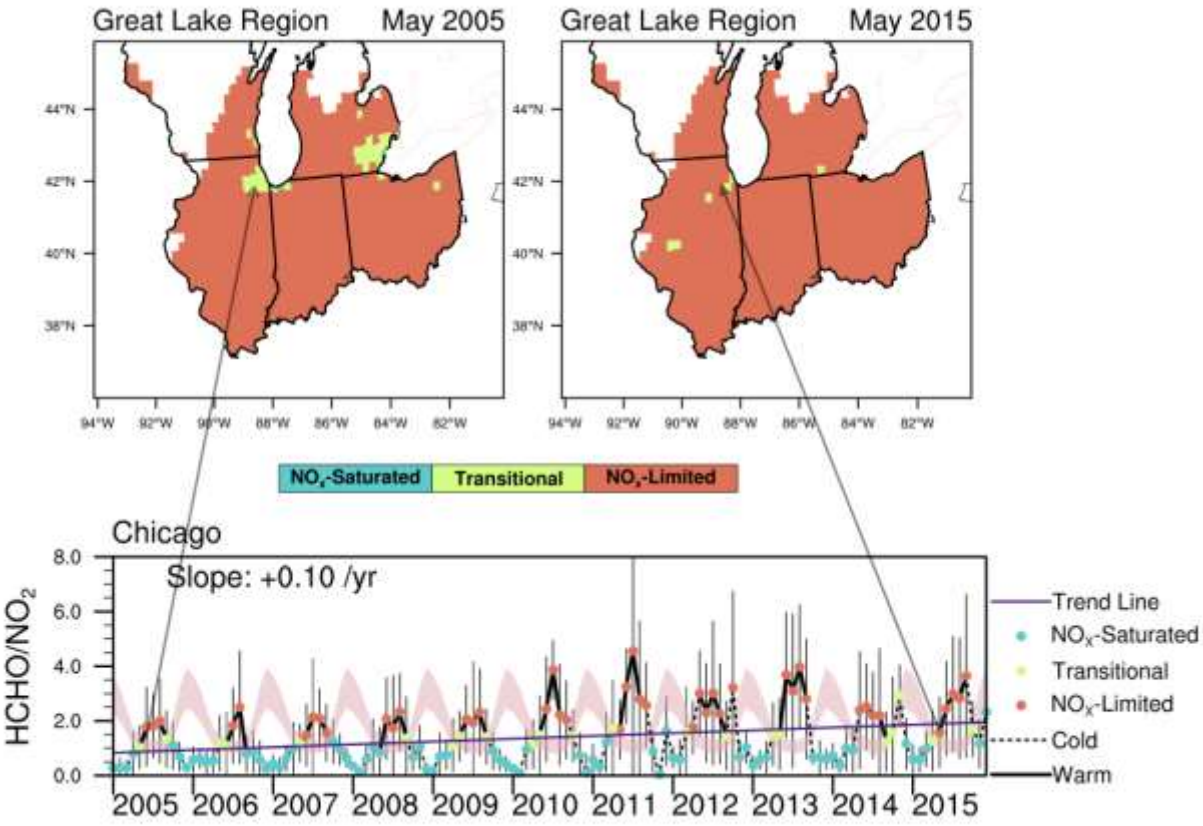

1132

1133 Figure 9 Same as Figure 8 but for Great Lake Region and Chicago.

1134

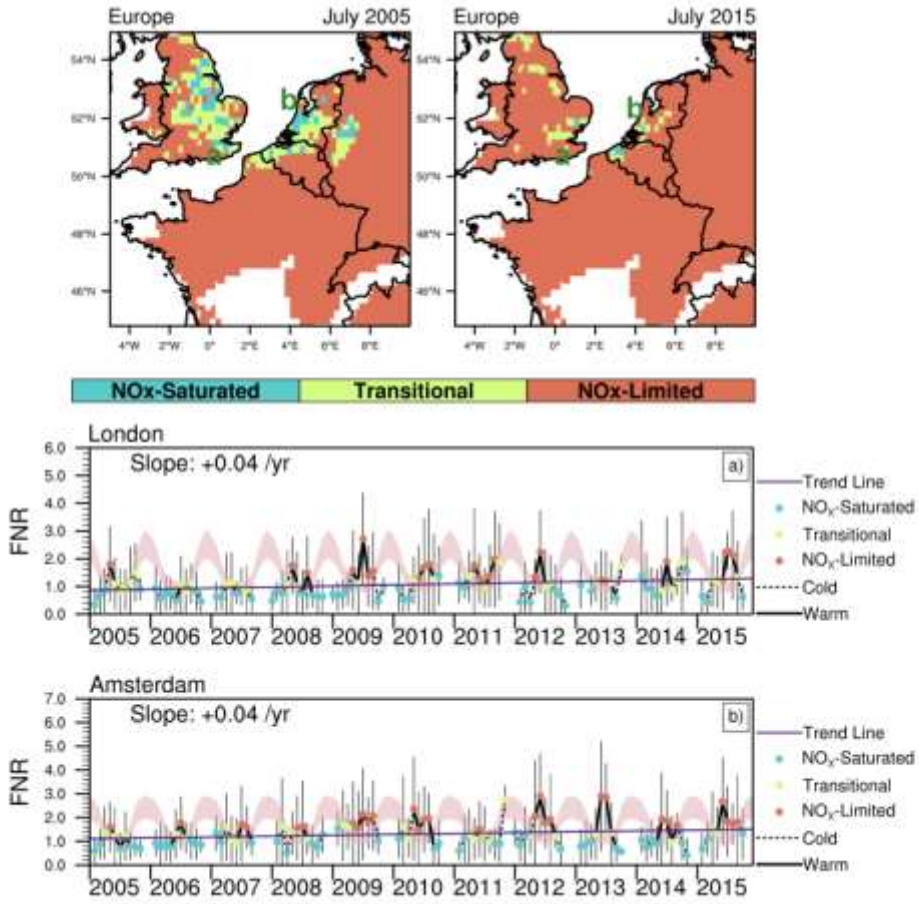

Figure 10 Same as Figure 8 but for Central Europe in July 2005 and 2015 (top), and time series in London (a) and Amsterdam (b). The letters mark the approximate location of London and Amsterdam. Missing values indicate no sufficient valid observations during the month.

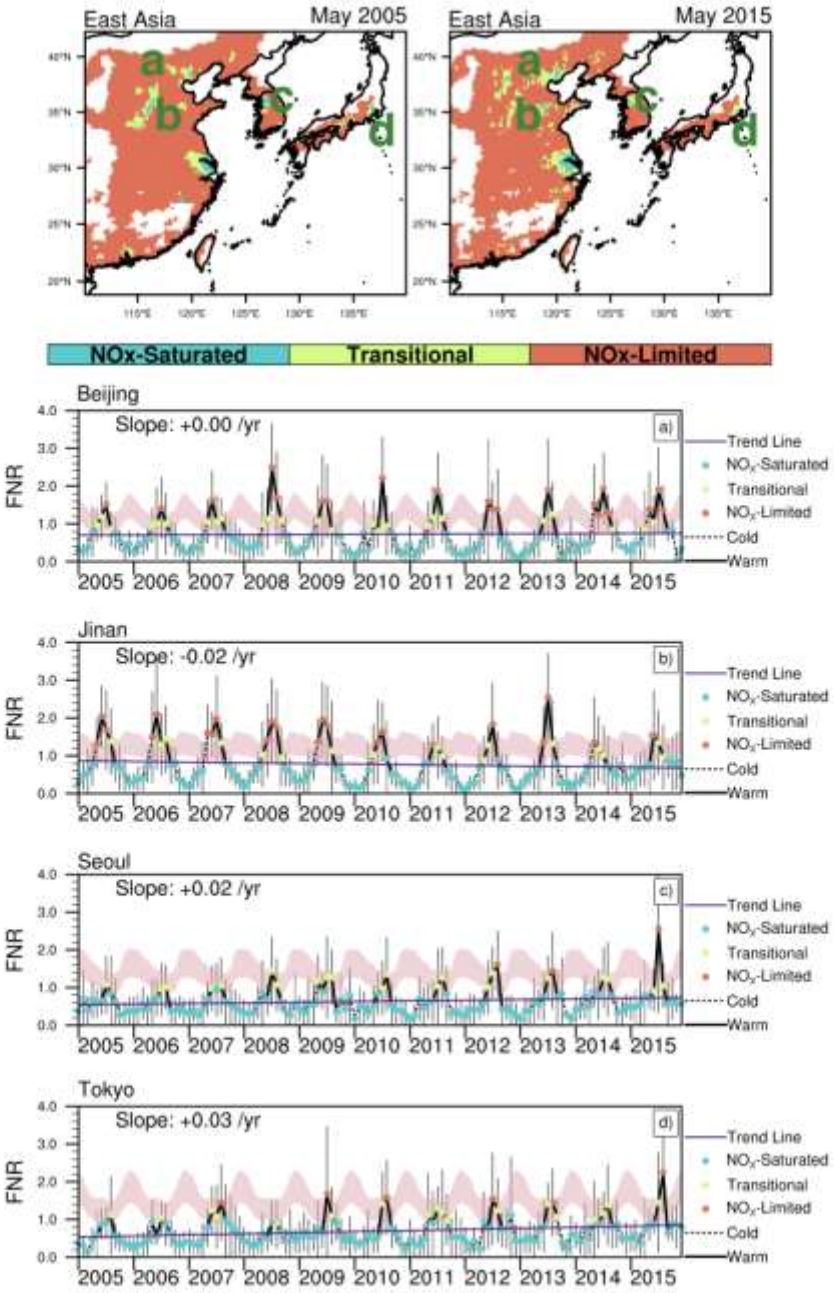

1140

1141 Figure 11 Same as Figure 8 but for East Asia in May 2005 and 2015 (top), and time series in
1142 Beijing (a), Jinan (b), Seoul (c), and Tokyo (d). The letters mark the approximate location of the
1143 four cities.

Table 1 Summary of previous studies that use surface or column $HCHO/NO_2$ as indicators of surface ozone sensitivity.

Reference	Study Area	Indicator Ratio	Regime Threshold Values	Model	Observation
Tonnesen *et al*., [2000]	New York City Area	Surface $HCHO/NO_2$	<0.8 NO_x-Saturated >1.8 NO_x-limited 0.8~1.8 Transition	RADM	Ground-based Measurements
Martin *et al*., [2004a]	North America, East Asia and Europe	Column $HCHO/NO_2$	<1.0 NO_x-Saturated >1.0 NO_x-limited	GEOS-Chem	GOME
Duncan *et al*., [2010]	U.S.	Column $HCHO/NO_2$	<1.0 NO_x-Saturated >2.0 NO_x-limited 1.0~2.0 Transition	NASA LaRC	OMI
Choi *et al*., [2012]	U.S.	Column $HCHO/NO_2$	<1.0 NO_x-Saturated >2.0 NO_x-limited 1.0~2.0 Transition	CMAQ	GOME
Chang *et al*., [2016]	Northeast U.S.	Column $HCHO/NO_2$	<1.5 NO_x-Saturated >2.3 NO_x-limited 1.5~2.3 Transition	CMAQ-DDM	OMI
Jin and Holloway [2015]	China	Column $HCHO/NO_2$	<1.0 NO_x-Saturated >2.0 NO_x-limited 1.0~2.0 Transition	N/A	OMI

Table 2 Comparison between OMI FNR and GEOS-Chem modeled FNR. Mean bias is the averaged difference between OMI observed minus model retrievals. Agreement is defined as the percentage of both FNR_{GC} and FNR_{OMI} falling in the same photochemical regime. Warm season includes May to September, and cold season includes October to April.

		Mean Bias	**R**	**Agreement (warm)**	**Agreement (cold)**
North America	**FNR_{GC} *vs.* FNR_{OMI_SS}**	-25%	0.74	94%	78%
	FNR_{GC} *vs.* FNR_{OMI_BS}	17%	0.74	97%	74%
	FNR_{GC} *vs.* FNR_{OMI_BD}	17%	0.63	97%	70%
	FNR_{GC} *vs.* FNR_{OMI_SD}	-26%	0.61	94%	76%
	FNR_{GC} *vs.* $FNR_{OMI\_BS\_L3}$	10%	0.56	96%	67%
Europe	**FNR_{GC} *vs.* FNR_{OMI_SS}**	-18%	0.44	83%	73%
	FNR_{GC} *vs.* FNR_{OMI_BS}	28%	0.61	90%	63%
	FNR_{GC} *vs.* FNR_{OMI_BD}	33%	0.44	90%	63%
	FNR_{GC} *vs.* FNR_{OMI_SD}	-15%	0.28	83%	71%
	FNR_{GC} *vs.* $FNR_{OMI\_BS\_L3}$	33%	0.44	90%	56%
East Asia	**FNR_{GC} *vs.* FNR_{OMI_SS}**	-30%	0.68	80%	83%
	FNR_{GC} *vs.* FNR_{OMI_BS}	10%	0.72	88%	74%
	FNR_{GC} *vs.* FNR_{OMI_BD}	39%	0.53	89%	70%
	FNR_{GC} *vs.* FNR_{OMI_SD}	-10%	0.47	85%	81%
	FNR_{GC} *vs.* $FNR_{OMI\_BS\_L3}$	17%	0.65	86%	74%

1155 Table 3 Comparison with previous *in-situ* ground-based studies over individual sites. The ozone
1156 production regime is derived from monthly average FNR using OMI Level-3 BIRA HCHO to
1157 Level-3 NASA SP NO_2.

Period	Study Area	Ozone Sensitivity	This Study	Method and Reference
July, 2005	Beijing	Urban: NO_x-saturated Rural: NO_x-Limited	Urban: Transitional to NO_x-limited Rural: NO_x-Limited	CMAQ-RSM [*Xing et al*., 2011]
July, 2005	Shanghai			
July, 2005	Guangzhou			
Nov., 2007	Guangzhou	NO_x-saturated	NO_x-saturated	Photochemical trajectory model [*Cheng et al*., 2010]
June – July, 2005	Beijing	NO_x-limited or Transitional	Transitional	Ground-based Measurements [*Wang et al.*, 2006]
June - July, 2006	Lanzhou	NO_x-limited	NO_x-limited	Observation-based model (MCM3.2) [*Xue et al*., 2014]
May - June, 2005	Shanghai	NO_x-saturated	Transitional	
Aug., 2006	Beijing	Mixed s	Transitional	Observation-based photochemical box model (OBM) [*Lu et al.*, 2010]
Nov., 2006	PRD	Mixed	Rural: NOx-Limited Urban: NO_x-saturated	Chemical Transport Model (EBM) [*Li et al*., 2013]
Aug., 2007	Beijing	Transitional	Transitional	1-D photochemical model [*Liu et al.*, 2012]
Nov., 2008	PRD	NO_x-saturated	NO_x-saturated	WRF-Chem [*Ye et al.*, 2016]
May - June, 2010	Jiangsu	Mixed	NO_x-saturated	Observation-based model (RACM) [*Pan et al*., 2015]
Summer 2009 - 2011	Miyun Site (Beijing)	NO_x-saturated	Transitional to NO_x-limited	Smog Production algorithm (OBM) [*Wang et al.*, 2008]
2009-2011	Seoul	NO_x-saturated	NO_x-saturated or Transitional	Statistical Correlation Analysis [*Iqbal et al.*, 2014]
May - Oct., 2006	Houston	NO_x-Limited	NO_x-Limited	CAMx [*Kommalapati et al.*, 2016]
Summer 2008-2009	Chicago	NO_x-saturated	NO_x-Limited	Statistical trend analysis [*Jing et al.*, 2014]
2007	Sacramento, CA	NO_x-Limited or Transitional	NO_x-Limited or Transitional	Observation-based 1-D plume model [*LaFranchi et al.*, 2011]
2007-2010	Southern and Central San Joaquin Valley	NO_x-Limited	NO_x-Limited	Observation-based method [*Pusede et al*., 2012]
2007-2010	Northern San Joaquin Valley	NO_x-saturated	NO_x-Limited	
Sept., 2013	Houston	Mostly NO_x-Limited (afternoon)	NO_x-Limited	Observation-based model (CB05) [*Mazzuca et al*., 2016]

1158
1159
1160

1161
1162

Figure 1.

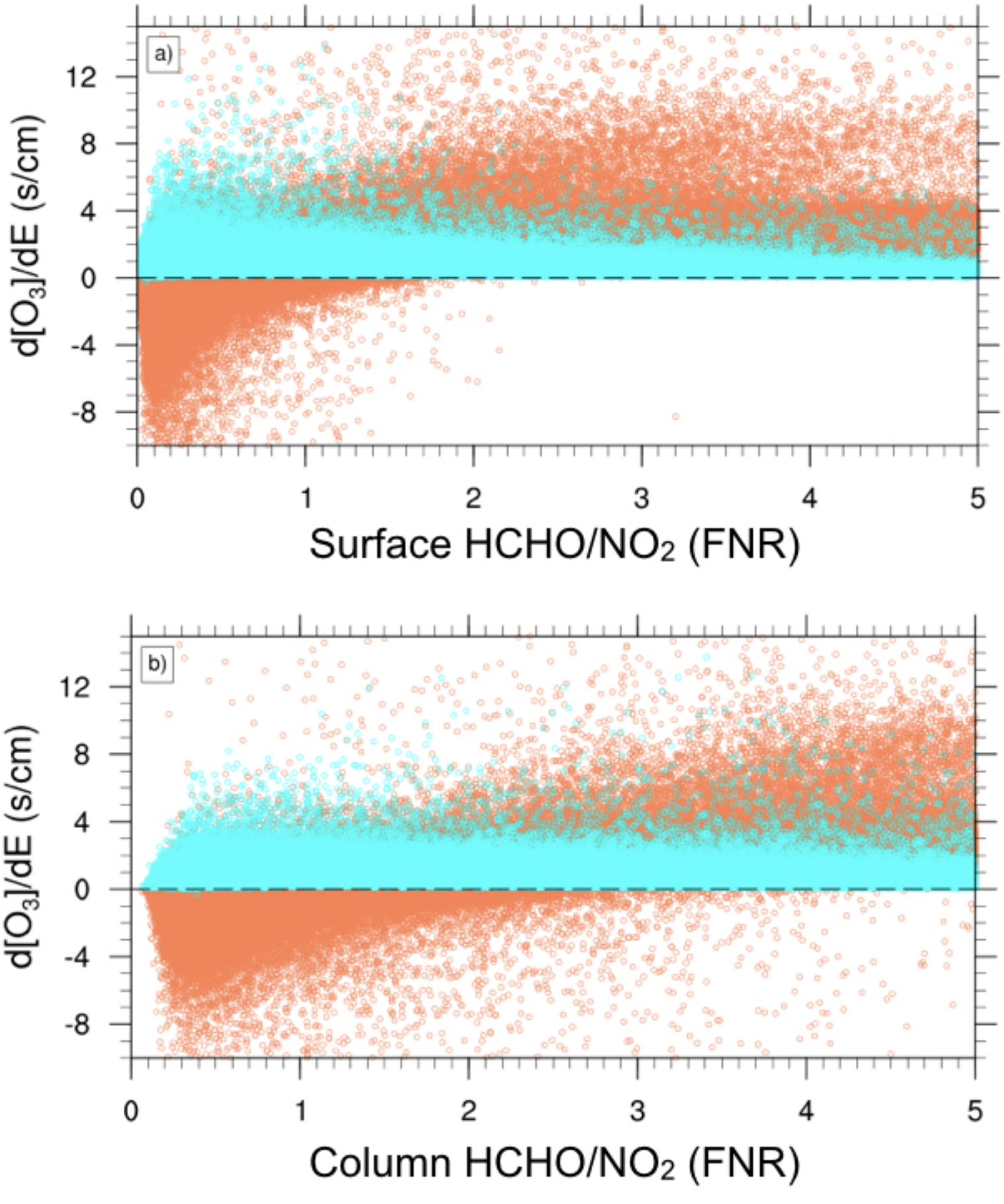
a)
12
8
4
0
-4
-8
d[O3]/dE (s/cm)
0
1
2
3
4
5
Surface HCHO/NO2 (FNR)
b)
12
8
4
0
-4
-8
d[O3]/dE (s/cm)
0
1
2
3
4
5
Column HCHO/NO2 (FNR)

Figure 2.

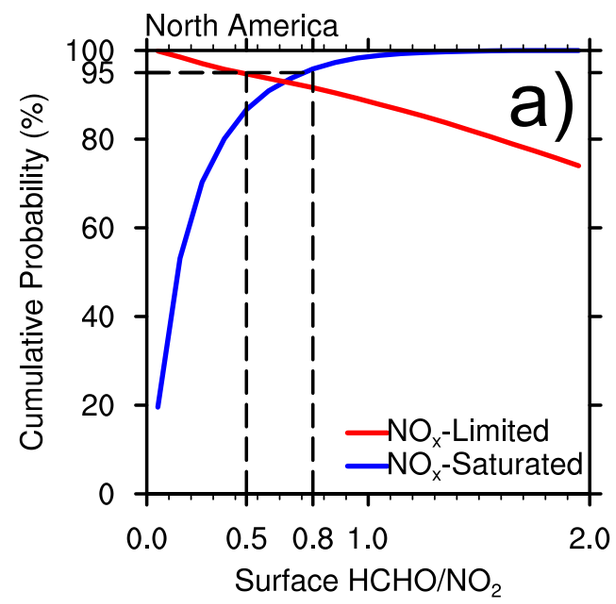
North America
a)
Cumulative Probability (%)
100
95
80
60
40
20
0
0.0
0.5
0.8
1.0
2.0
Surface HCHO/NO2
NOx-Limited
NOx-Saturated

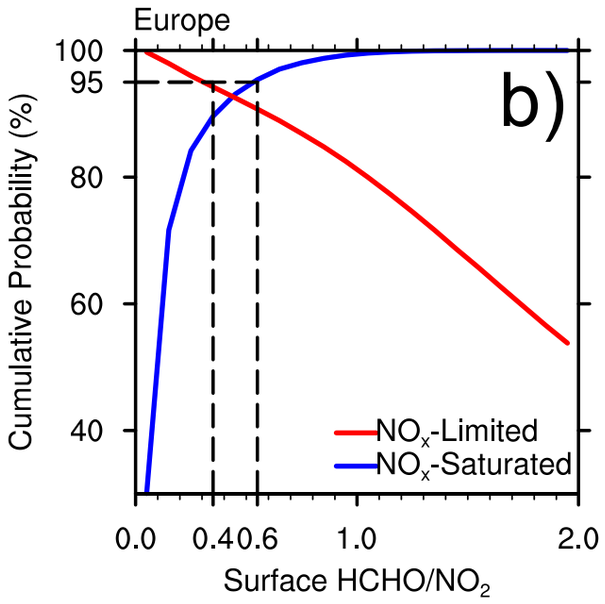
Europe
b)
Cumulative Probability (%)
100
95
80
60
40
0.0
0.4
0.6
1.0
2.0
Surface HCHO/NO2
NOx-Limited
NOx-Saturated

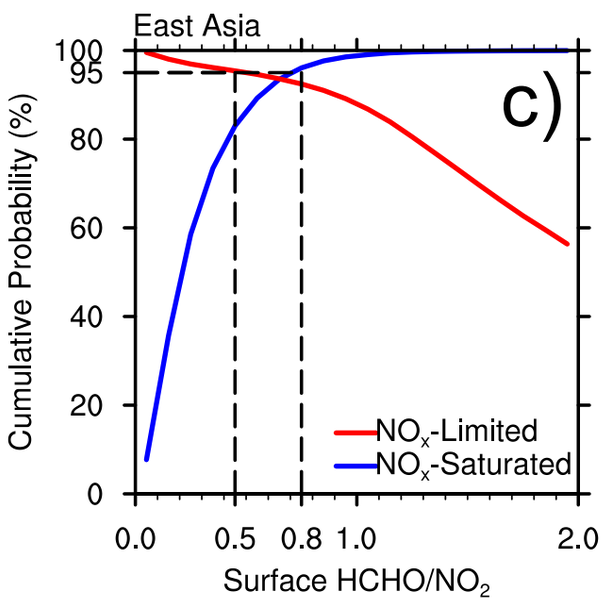
East Asia
c)
Cumulative Probability (%)
100
95
80
60
40
20
0
0.0
0.5
0.8
1.0
2.0
Surface HCHO/NO2
NOx-Limited
NOx-Saturated

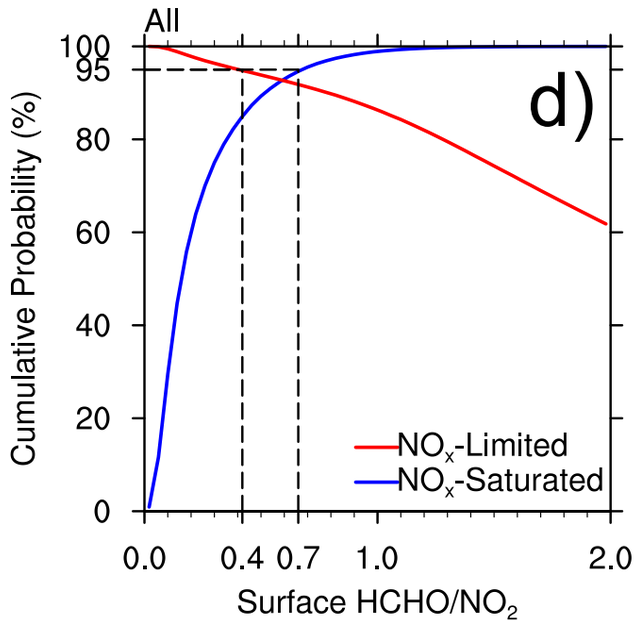
All
d)
Cumulative Probability (%)
100
95
80
60
40
20
0
0.0
0.4
0.7
1.0
2.0
Surface HCHO/NO2
NOx-Limited
NOx-Saturated

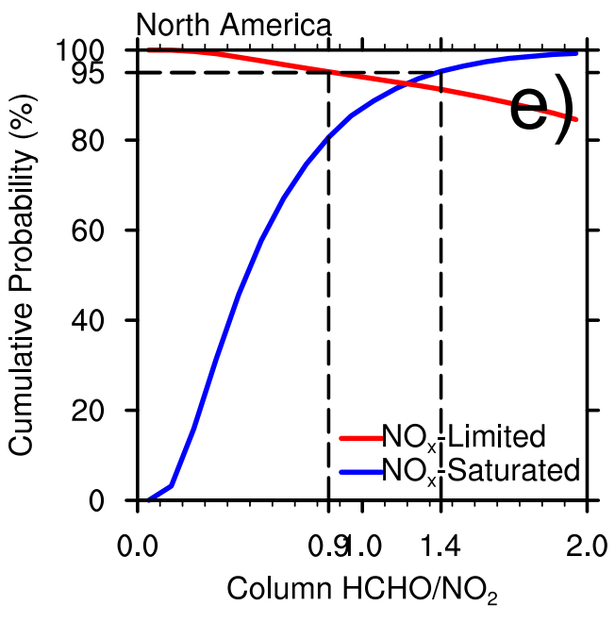
North America
e)
Cumulative Probability (%)
100
95
80
60
40
20
0
0.0
0.9
1.0
1.4
2.0
Column HCHO/NO2
NOx-Limited
NOx-Saturated

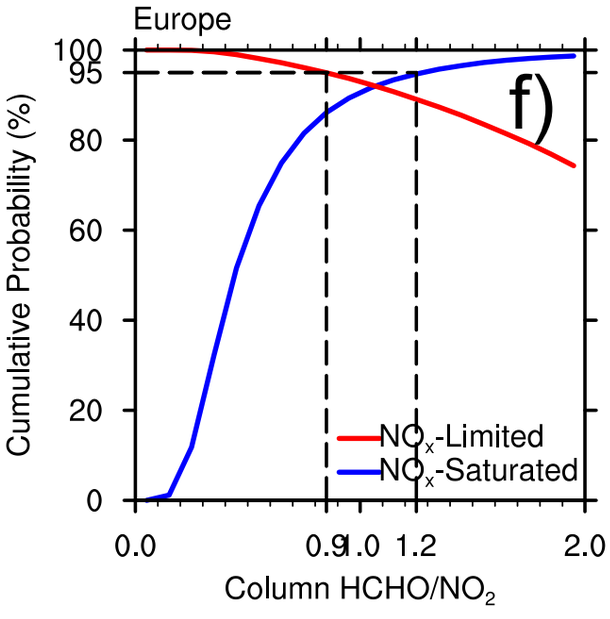
Europe
f)
Cumulative Probability (%)
100
95
80
60
40
20
0
0.0
0.9
1.0
1.2
2.0
Column HCHO/NO2
NOx-Limited
NOx-Saturated

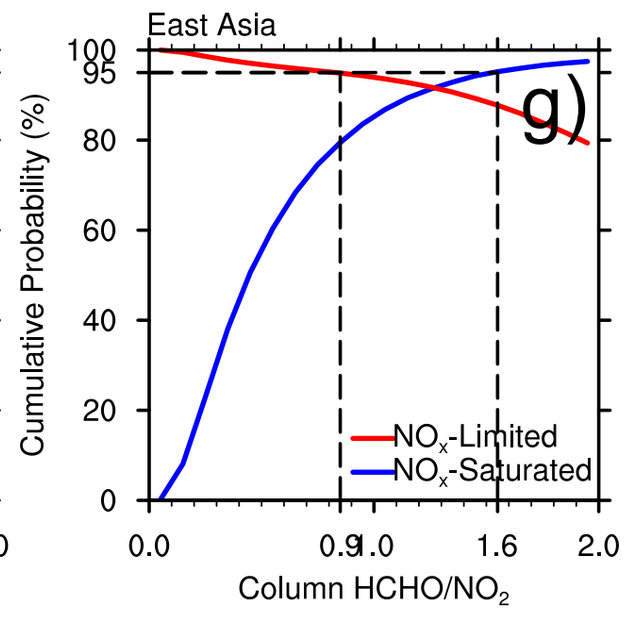
East Asia
g)
Cumulative Probability (%)
100
95
80
60
40
20
0
0.0
0.9
1.0
1.6
2.0
Column HCHO/NO2
NOx-Limited
NOx-Saturated

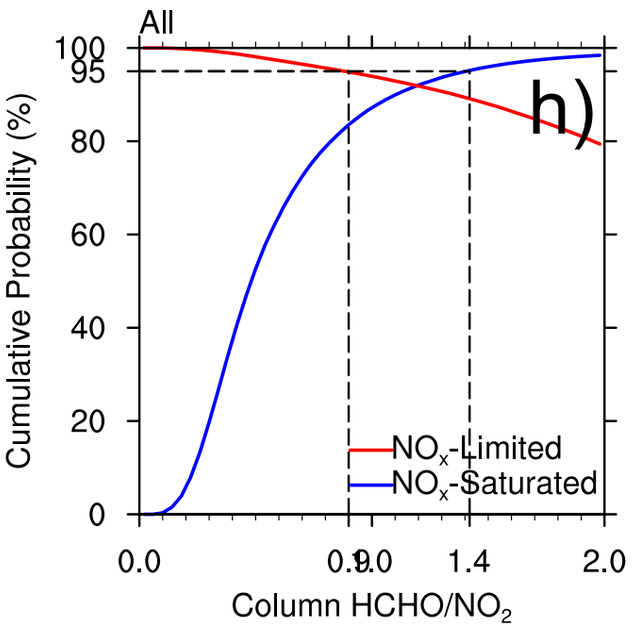
All
h)
Cumulative Probability (%)
100
95
80
60
40
20
0
0.0
0.9
1.0
1.4
2.0
Column HCHO/NO2
NOx-Limited
NOx-Saturated

Figure 3.

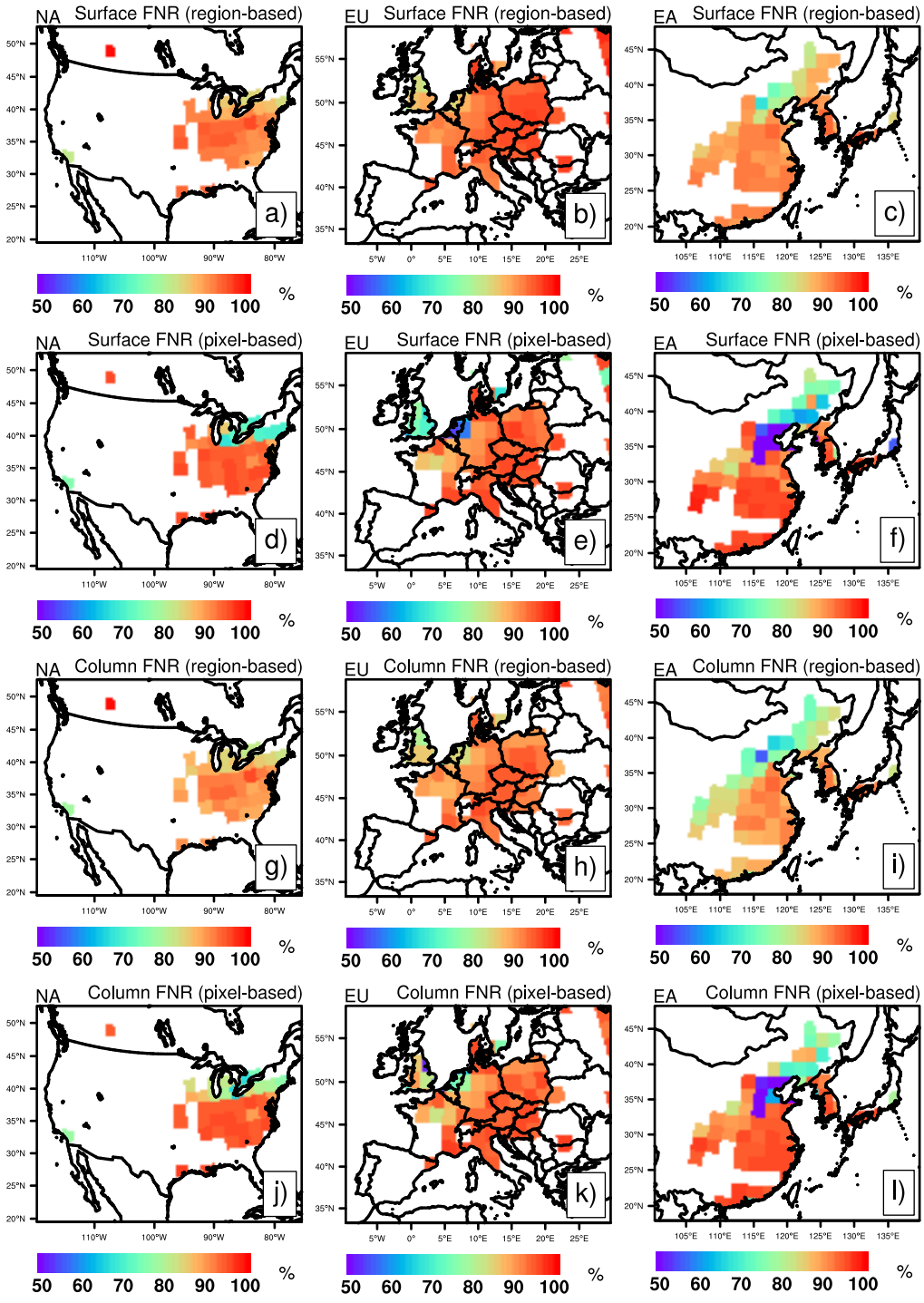
NA Surface FNR (region-based)
EU Surface FNR (region-based)
EA Surface FNR (region-based)
NA Surface FNR (pixel-based)
EU Surface FNR (pixel-based)
EA Surface FNR (pixel-based)
NA Column FNR (region-based)
EU Column FNR (region-based)
EA Column FNR (region-based)
NA Column FNR (pixel-based)
EU Column FNR (pixel-based)
EA Column FNR (pixel-based)
a)
b)
c)
d)
e)
f)
g)
h)
i)
j)
k)
l)
50 60 70 80 90 100
%

Figure 4.

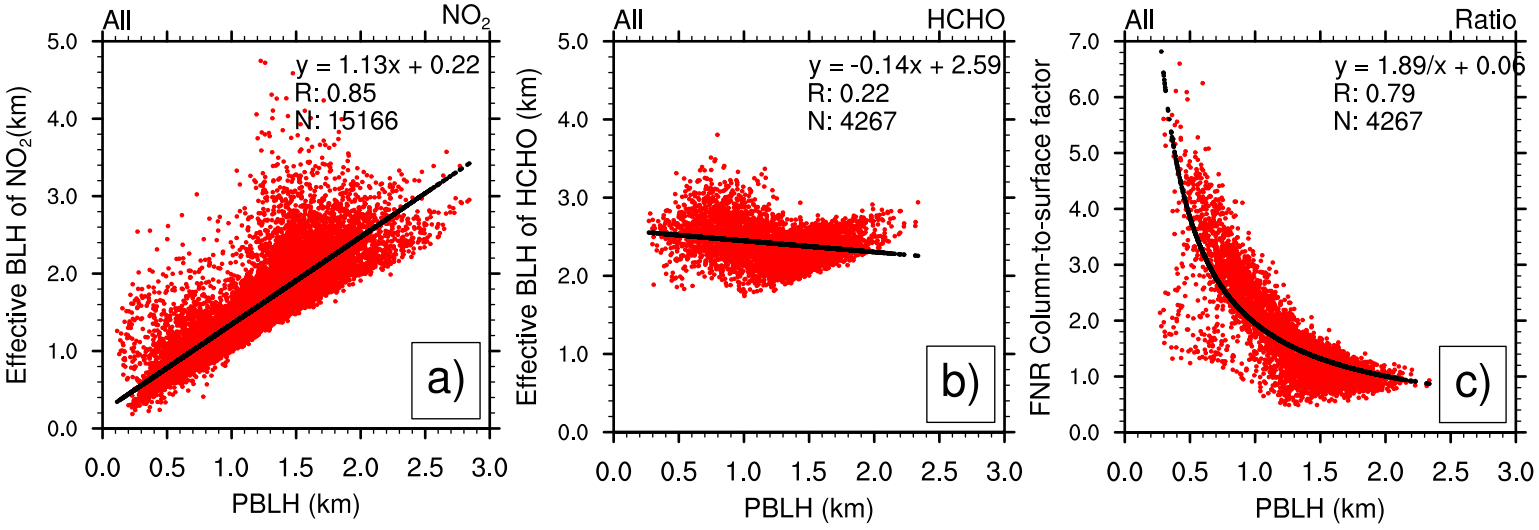
All
NO2
y = 1.13x + 0.22
R: 0.85
N: 15166
a)
Effective BLH of NO2(km)
PBLH (km)
All
HCHO
y = -0.14x + 2.59
R: 0.22
N: 4267
b)
Effective BLH of HCHO (km)
PBLH (km)
All
Ratio
y = 1.89/x + 0.06
R: 0.79
N: 4267
c)
FNR Column-to-surface factor
PBLH (km)

Figure 5.

Warm Season

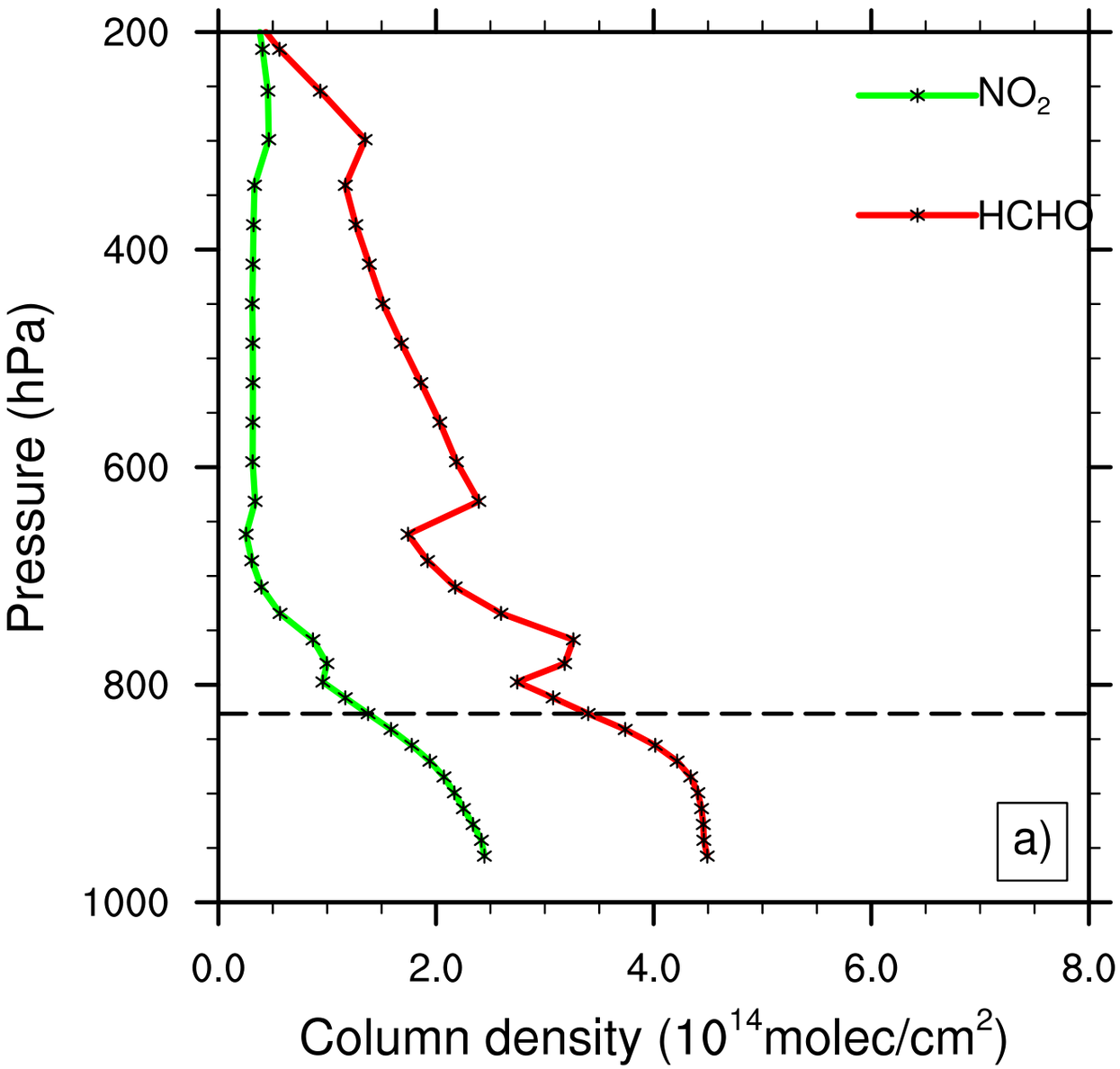

Cold Season

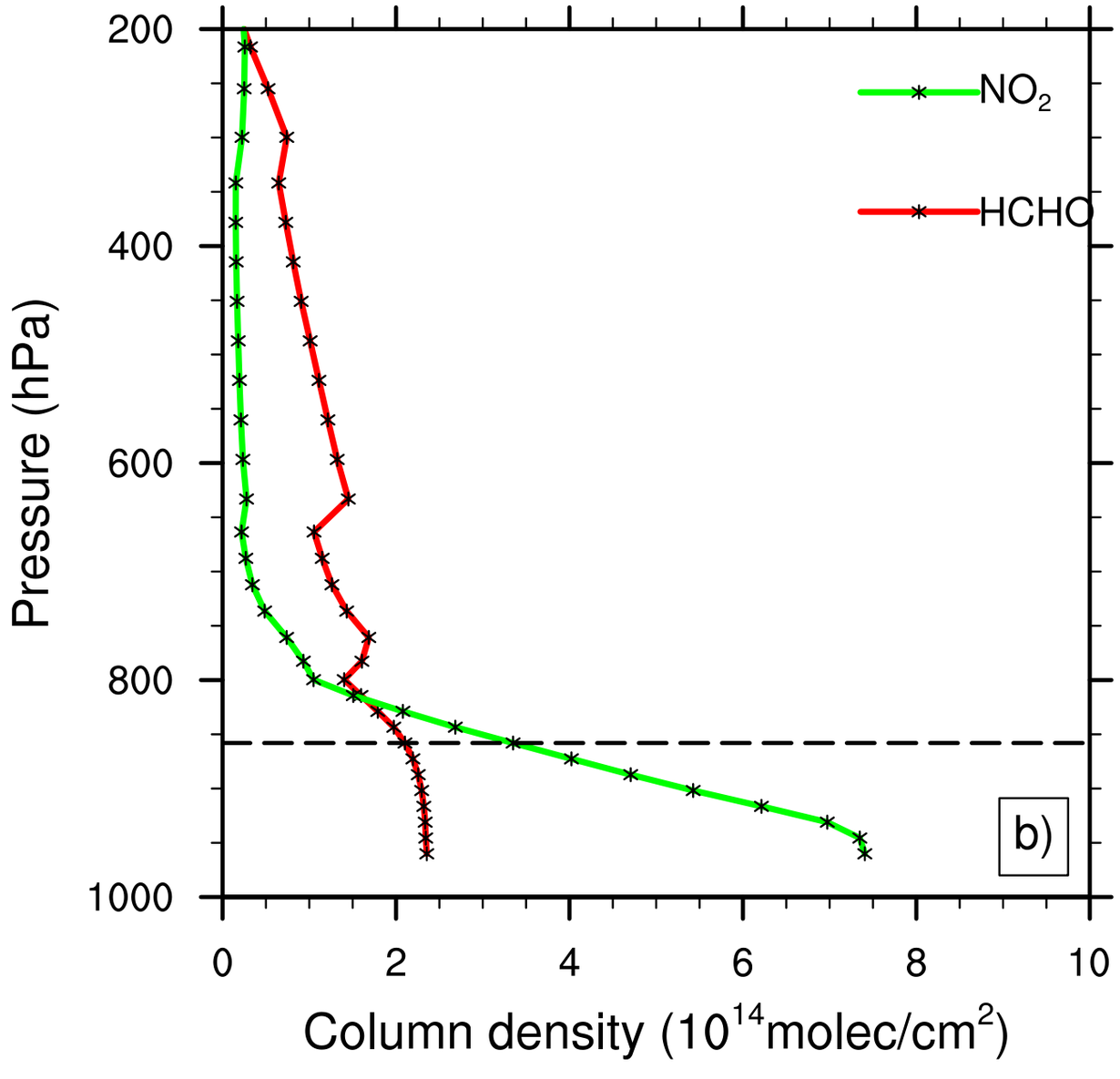

Figure 6.

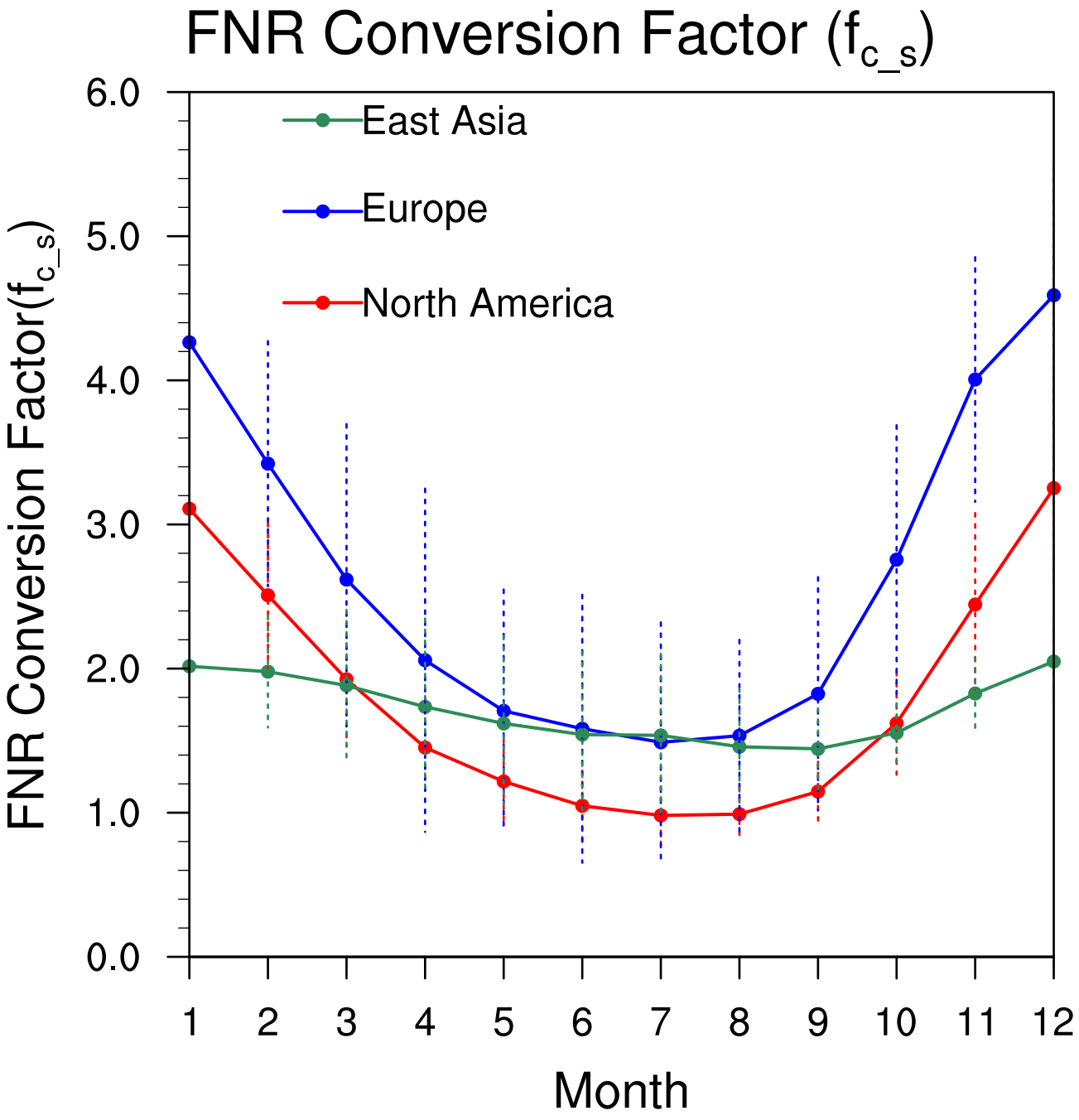
FNR Conversion Factor (f_{c_s})
East Asia
Europe
North America
FNR Conversion Factor(f_{c_s})
6.0
5.0
4.0
3.0
2.0
1.0
0.0
1
2
3
4
5
6
7
8
9
10
11
12
Month

Figure 7.

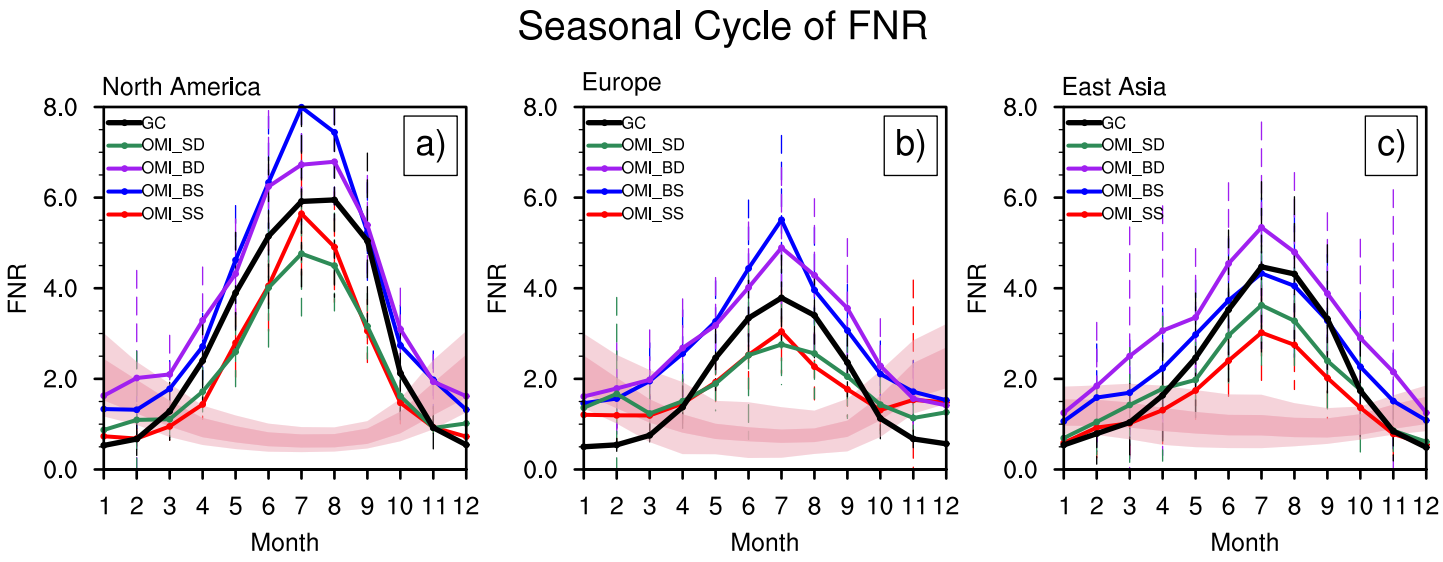
Seasonal Cycle of FNR
North America
Europe
East Asia
a)
b)
c)
GC
OMI_SD
OMI_BD
OMI_BS
OMI_SS
FNR
Month
0.0
2.0
4.0
6.0
8.0
1 2 3 4 5 6 7 8 9 10 11 12

Figure 8.

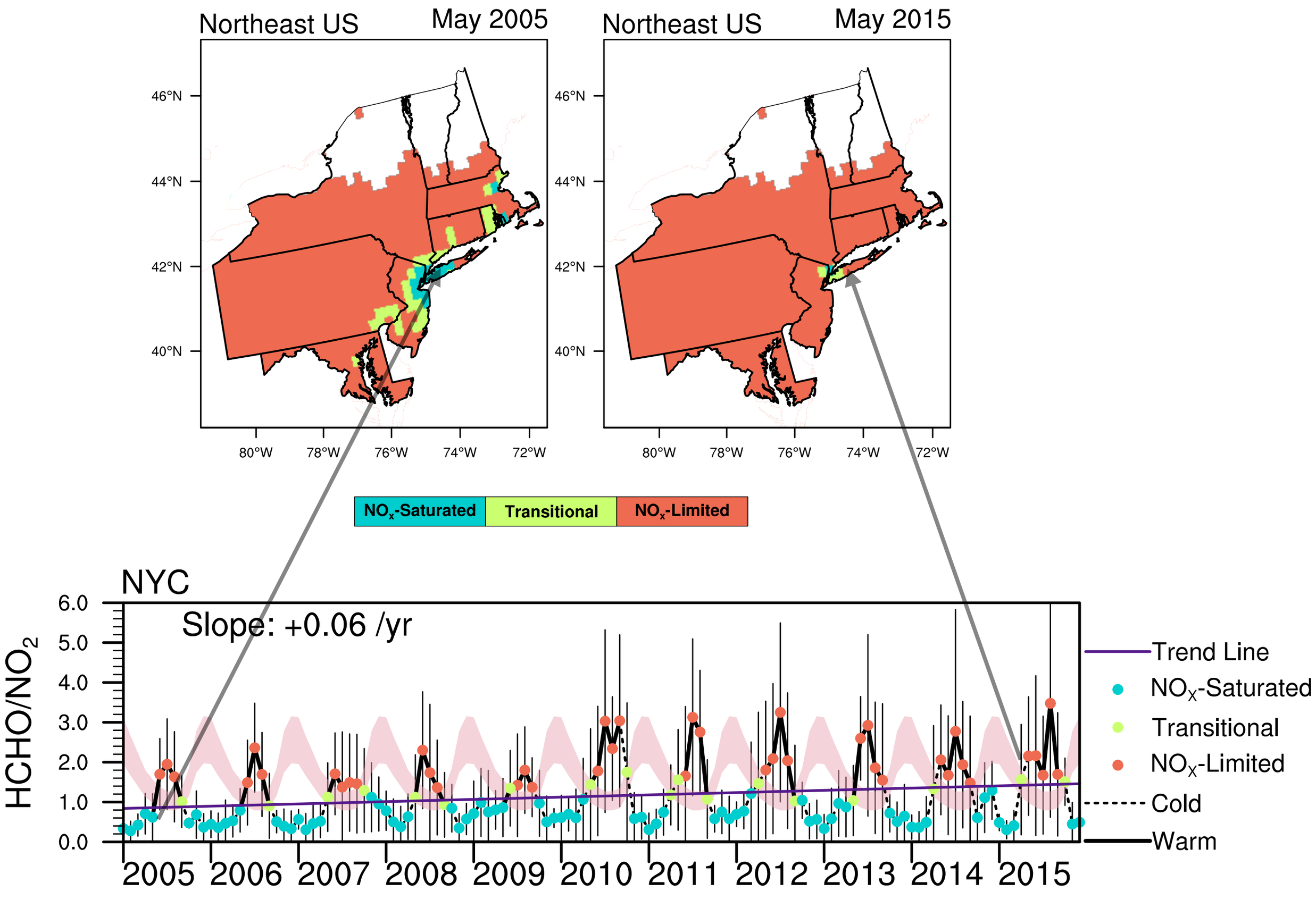
Northeast US
May 2005
Northeast US
May 2015
46°N
44°N
42°N
40°N
80°W
78°W
76°W
74°W
72°W
NOx-Saturated
Transitional
NOx-Limited
NYC
Slope: +0.06 /yr
HCHO/NO2
6.0
5.0
4.0
3.0
2.0
1.0
0.0
2005
2006
2007
2008
2009
2010
2011
2012
2013
2014
2015
Trend Line
NOX-Saturated
Transitional
NOX-Limited
Cold
Warm

Figure 9.

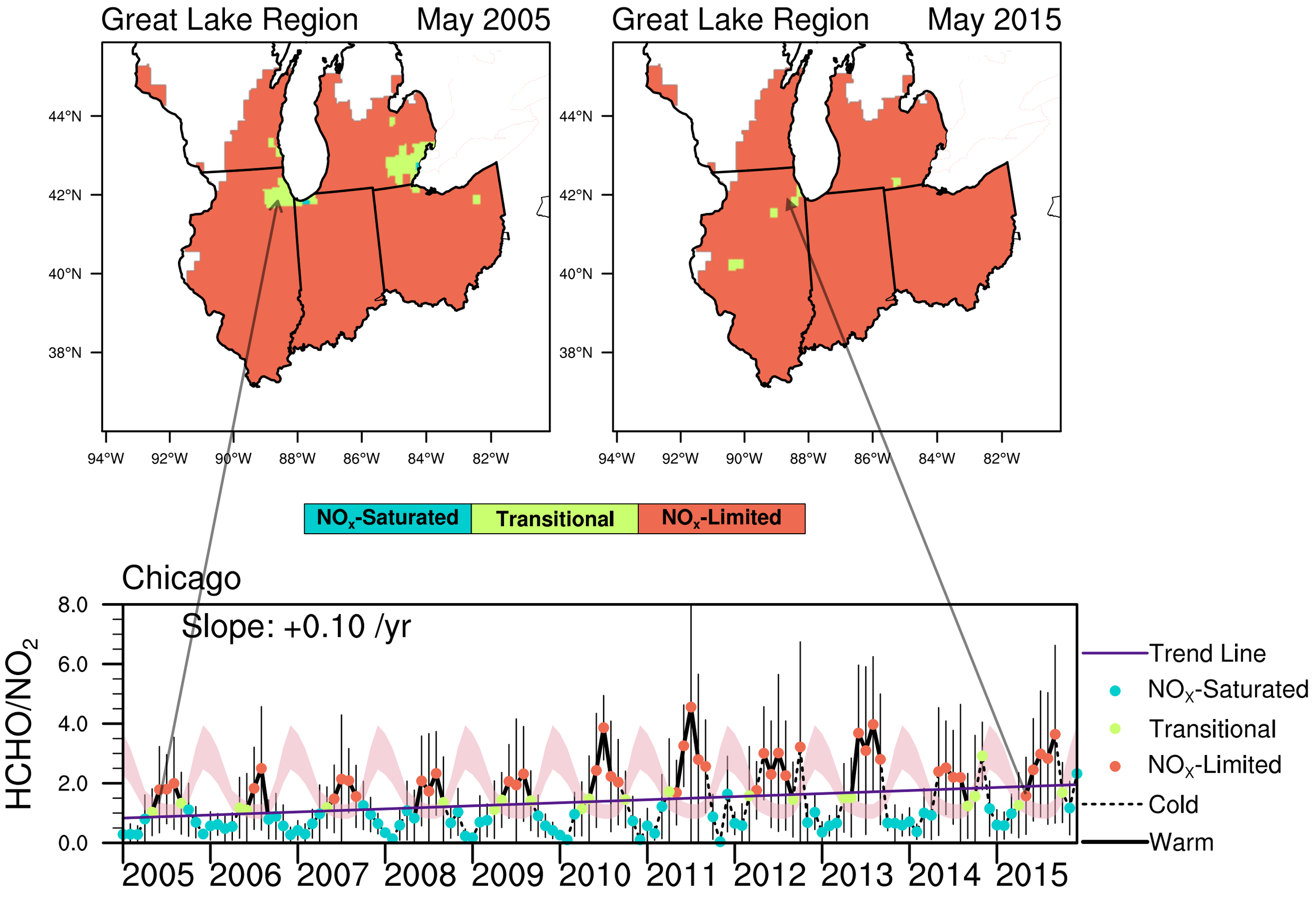
Great Lake Region
May 2005
Great Lake Region
May 2015
44°N
42°N
40°N
38°N
94°W
92°W
90°W
88°W
86°W
84°W
82°W
NOx-Saturated
Transitional
NOx-Limited
Chicago
Slope: +0.10 /yr
HCHO/NO2
8.0
6.0
4.0
2.0
0.0
2005
2006
2007
2008
2009
2010
2011
2012
2013
2014
2015
Trend Line
NOX-Saturated
Transitional
NOX-Limited
Cold
Warm

Figure 10.

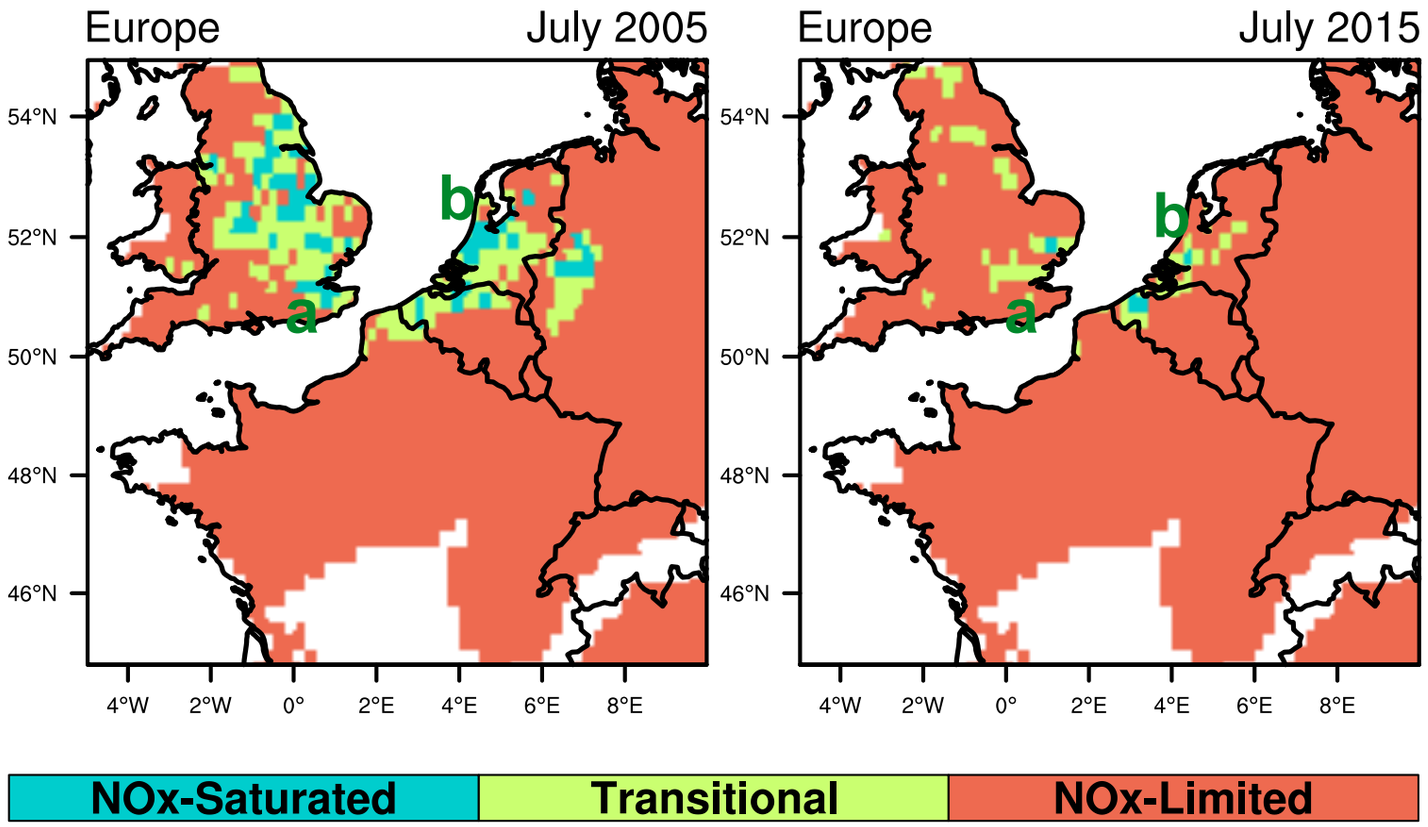
Europe
July 2005
Europe
July 2015
54°N
52°N
50°N
48°N
46°N
4°W
2°W
0°
2°E
4°E
6°E
8°E
a
b
NOx-Saturated
Transitional
NOx-Limited

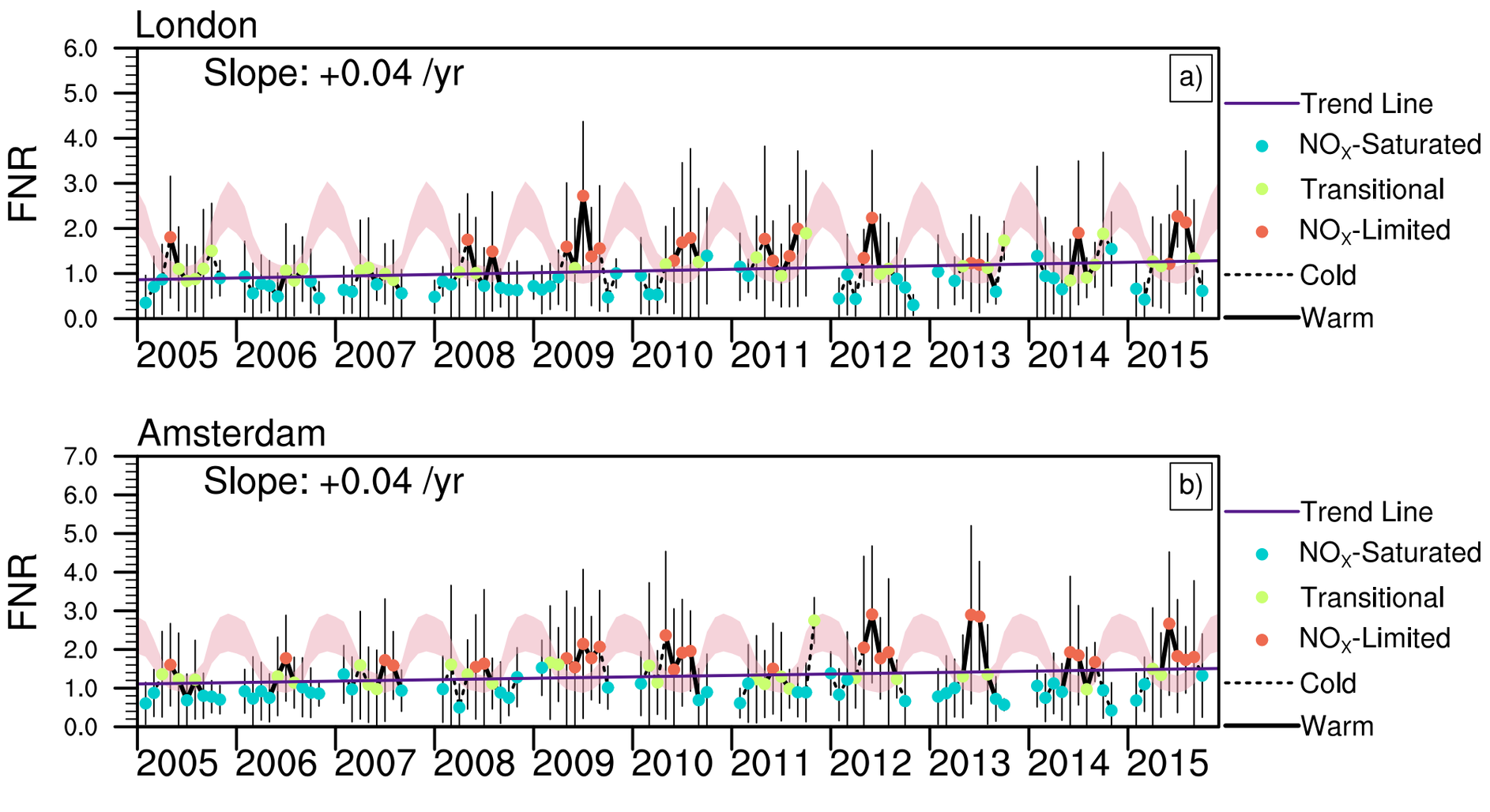
London
Slope: +0.04 /yr
a)
FNR
Trend Line
NOX-Saturated
Transitional
NOX-Limited
Cold
Warm
2005
2006
2007
2008
2009
2010
2011
2012
2013
2014
2015
Amsterdam
Slope: +0.04 /yr
b)

Figure 11.

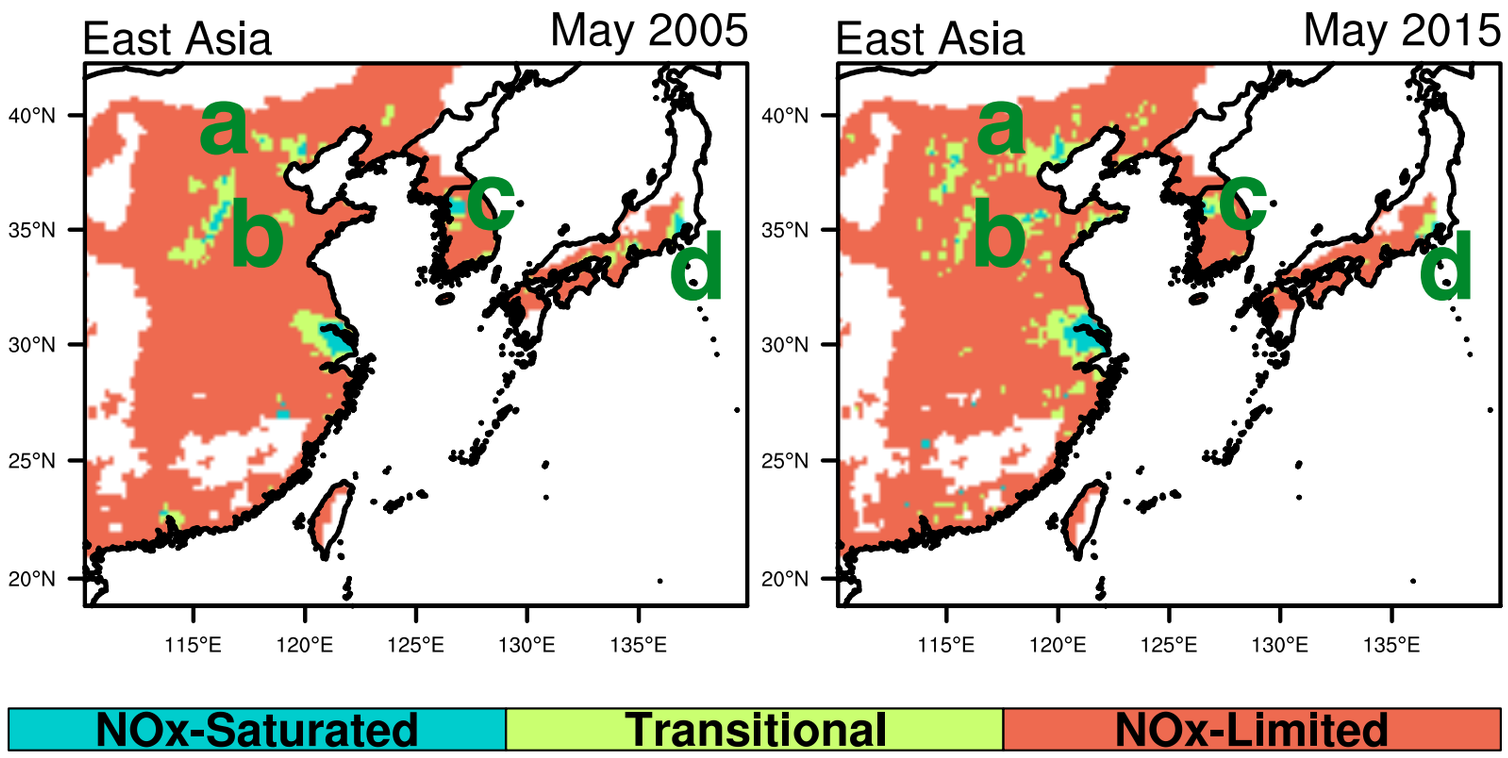
East Asia
May 2005
East Asia
May 2015
a
b
c
d
40°N
35°N
30°N
25°N
20°N
115°E
120°E
125°E
130°E
135°E
NOx-Saturated
Transitional
NOx-Limited

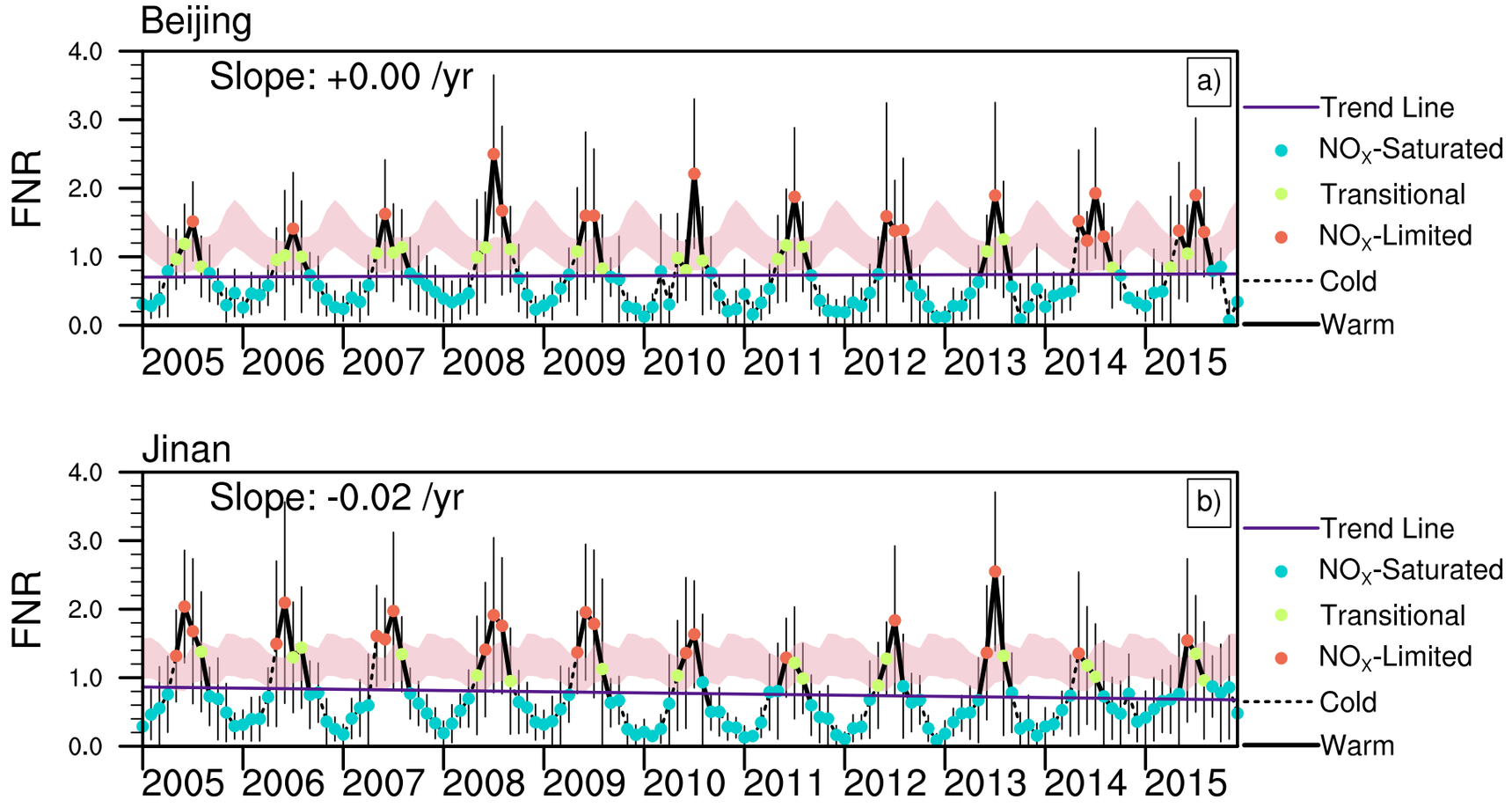
Beijing
Slope: +0.00 /yr
a)
Jinan
Slope: -0.02 /yr
b)
Seoul
Slope: +0.02 /yr
c)
Tokyo
Slope: +0.03 /yr
d)
FNR
4.0
3.0
2.0
1.0
0.0
2005 2006 2007 2008 2009 2010 2011 2012 2013 2014 2015
Trend Line
NOX-Saturated
Transitional
NOX-Limited
Cold
Warm